

This is the accepted manuscript version of the contribution published as:

Clarke, D.B., Harlov, D.E., Brenan, J.M., **Jähkel, A.**, Cichy, S.B., Wilke, F.D.H., Yang, X. (2023):

Assimilation of xenocrystic apatite in peraluminous granitic magmas

Am. Miner. **108** (8), 1421 - 1435

The publisher's version is available at:

<https://doi.org/10.2138/am-2022-8668>

REVISION 1

Assimilation of xenocrystic apatite in peraluminous granitic magmas

Word Count: 11800

D. BARRIE CLARKE¹, DANIEL E. HARLOV^{2,3,4}, JAMES M. BRENNAN¹, ANNE JÄHKEL⁵,
SARAH B. CICHY^{2,6}, FRANZISKA D.H. WILKE², XIANG YANG⁷

¹ Department of Earth and Environmental Science, Dalhousie University, Halifax, NS, Canada
B3H 4R2

² Deutsches GeoForschungsZentrum GFZ, Telegrafenberg, 14473 Potsdam, Germany

³ Department of Geology, University of Johannesburg P.O. Box 524, Auckland Park,
2006 South Africa

⁴ Faculty of Earth Resources, China University of Geosciences, 430074 Wuhan, China

⁵ Departments Hydrogeologie / Aquatische Ökosystemanalyse, Helmholtz-Zentrum für
Umweltforschung GmbH – UFZ, 39114 Magdeburg, Germany

⁶ Institute for Geosciences, University of Potsdam, 14476 Potsdam-Golm, Germany

⁷ Department of Geology, St. Mary's University, Halifax, NS, Canada B3H 3C3

Barrie Clarke: clarke@dal.ca

Daniel Harlov: धारlov@gfz-potsdam.de

James Brennan: jbrenan@dal.ca

Anne Jähkel: anne.jaehkel@ufz.de

Sarah Cichy: cichy@uni-potsdam.de

Franziska Wilke: fwilke@gfz-potsdam.de

Xiang Yang: xiang.yang@smu.ca

33

34

ABSTRACT

35 Apatite is a ubiquitous phase in granite plutons and in most adjacent country rocks, thus
36 contamination of a granite magma with wall-rock material results in two genetic types of apatite
37 in the magma: cognate and foreign. These two textural and chemical varieties of apatite undergo
38 textural and compositional changes to reach physical and chemical equilibrium (perfect
39 assimilation) in the melt. Our experiments replicate the conditions in such contaminated granites.
40 The starting materials consist of a peraluminous synthetic $\text{SiO}_2\text{-Al}_2\text{O}_3\text{-Na}_2\text{O-K}_2\text{O}$ (SANK 1.3)
41 granite gel with A/NK of 1.3, synthetic F-apatite, synthetic Cl-apatite, and natural Durango
42 apatite. Initial experiments in cold-seal hydrothermal pressure vessels at magmatically realistic
43 temperatures of 750 °C and pressures of 200 MPa produced negligible reactions, even after run
44 times of 2000 h. Instead, we used an argon-pressurized internally heated pressure vessel with a
45 rapid-quench setup at temperatures of 1200 °C, pressures of 200 MPa, and run durations of 192
46 h. An advantage of this high temperature is that it exceeds the liquidus for quartz and feldspar;
47 therefore, apatite is the only solid phase in the run products. The starting composition of each run
48 was 90 wt.% SANK 1.3 granite gel and 10 wt.% crushed apatite (consisting of one, two, or three
49 varieties), with and without 4 wt.% added H_2O . Run products were examined by SEM for texture
50 and by EMPA and LA-ICP-MS for composition. The starting synthetic granite composition
51 contains no Ca, F, Cl, or REEs thus, in every run, apatite was initially undersaturated in the melt.
52 In all experiments, most large apatite grains consisted of anhedral shards with rounded corners,
53 most small apatite grains were round, and a small proportion of apatite grains developed one or
54 more crystal faces. In experiments with two or three apatite compositions, the run-product apatite
55 grains had compositions intermediate between those of the starting-material grains, and they

56 were homogeneous with respect to Cl, and probably F, but not with respect to REEs. The
57 processes to reach textural equilibrium consist of dissolution until the melt is saturated in apatite,
58 followed by Ostwald ripening to eliminate small grains and to develop crystal faces on larger
59 ones. The processes to reach chemical equilibrium consist of dissolution of apatite, diffusion of
60 cations (Ca, P, REE) and anions (F, Cl, OH) through the silicate melt, and solid-state diffusion in
61 the undissolved apatite grains. The halogens approached chemical equilibrium in all
62 experiments, but in the experiments containing Durango apatite, the REEs have not. Models
63 involving radial diffusion into spherical apatite grains at the temperatures of the experiments
64 show complete re-equilibration of the halogens, but changes in the REE concentrations affecting
65 only the outer few micrometers. We conclude that the rate of chemical equilibrium for the
66 halogens is greater than the rate of physical equilibrium for texture, which in turn is greater the
67 rate of chemical equilibrium for REEs. We illustrate these processes with a natural example of
68 contaminated granite from the South Mountain Batholith in Nova Scotia. Given that all granites
69 are contaminated rocks, we propose that future petrogenetic studies focus on developing
70 techniques for a minerals-based quantitative estimation of contamination (QEC).

71

72 **Keywords:** apatite, granite, chlorine, fluorine, REE, diffusion, equilibration, South Mountain
73 Batholith

74 Running Title: Assimilation of xenocrystic apatite in peraluminous granitic magmas

75

76

INTRODUCTION

77 In forensic science, Locard's Principle states that any physical contact between two
78 objects necessitates a transfer of material between them. In geological science, all granites are in
79 physical contact with their wall rocks, *ergo* all granites must have exchanged material with the
80 wall rocks, to varying extents. Country-rock xenoliths, country-rock xenocrysts, and new
81 peritectic phases in the granites all represent physical manifestations of this contamination. If
82 these physically distinct contaminants are included in whole-rock chemical analyses, there
83 clearly must be a country-rock component in those measured compositions. If the contaminants
84 have been completely assimilated, with no physical evidence remaining, again the whole-rock
85 chemical composition will contain a country-rock component.

86 The uniformly peraluminous South Mountain Batholith (~375 Ma) of southwestern Nova
87 Scotia (MacDonald, 2001; Clarke, 2019) is a perfect natural laboratory in which to study the
88 effects of contamination. It is enveloped along more than 95% of its surface by 10-km thick
89 metagreywackes and metapelites of the Cambro-Ordovician Meguma Supergroup. The 15 most
90 abundant mineral species in the country rocks are identical to the 15 most abundant mineral
91 species in the batholith, but the proportions, compositions, and textures of these minerals are, of
92 course, significantly different. When mineral phase X from the country rock joins mineral phase
93 X in the granite magma, the two varieties of X undergo physical and chemical changes to reach
94 physical and chemical equilibrium by chemical exchange through the medium of the silicate melt
95 (Clarke, 2007). Ideally, to fully understand the contamination history of a granite, it is preferable
96 that the system has *not* reached equilibrium so that the contaminants are still physically and
97 chemically recognizable.

98 Over the last two decades, we have systematically studied the contamination in the South
99 Mountain Batholith from a mineralogical standpoint, one phase at a time, including garnet
100 ([Lackey et al., 2011](#)), cordierite ([Erdmann et al., 2004](#)), andalusite ([Clarke et al., 2005](#)), rutile
101 ([Carruzzo et al., 2006](#)), ilmenite ([Clarke and Carruzzo, 2007](#)), sulphides ([Clarke et al., 2009](#)), and
102 apatite ([Jähkel, 2010](#)).

103 The dual purposes of this study are to conduct experiments that simulate the
104 contamination of an apatite-bearing granite magma with foreign apatite, and to illustrate the
105 contamination and assimilation processes with an example from the South Mountain Batholith.
106 We demonstrate that a detailed assessment of the role of contamination, as revealed through a
107 careful examination of the mineralogy of individual phases, is essential to understand the
108 petrogenesis of granites.

109

110 **EXPERIMENTAL AND ANALYTICAL PROCEDURES**

111 **Apatite – peraluminous granite melt experiments**

112 We prepared a synthetic peraluminous $\text{SiO}_2\text{-Al}_2\text{O}_3\text{-Na}_2\text{O-K}_2\text{O}$ (SANK 1.3) granite gel
113 using tetra-ethyl orthosilicate (TEOS) and Al-Na-K nitrates ([Hamilton and Henderson, 1968](#);
114 [Rizkalla et al., 1991](#)). In this gel, the nominal $\text{K}_2\text{O/Na}_2\text{O}$ ratio is 1.2, and the nominal
115 peraluminosity $A/NK \approx 1.3$. Of special note is that this unfused starting gel contains none of the
116 chemical components of apatite (Ca-P-F-Cl-REE), similar to the apatite dissolution experiments
117 of [Wolf and London \(1994\)](#). The unfused SANK 1.3 gel was stored permanently in a drying
118 oven at 110 °C, but it may initially have contained some H_2O , considering that it is extremely

119 hygroscopic, and it could have gained more H₂O from the atmosphere during weighing, grinding,
120 and loading.

121 The apatite used in the experimental runs consisted of grains of synthetic fluorapatite
122 APS-64 (F-Ap), synthetic chlorapatite APS-65 (Cl-Ap), and natural Durango apatite (D-Ap).
123 The synthetic apatite compositions were synthesized using a variation of the molten flux method
124 outlined by [Schettler et al. \(2011\)](#) (see also [Cherniak, 2000](#)). [Xu et al. \(2020\)](#) reported the mean
125 major-element composition of the Durango apatite as (wt%): CaO 54.19; P₂O₅ 40.78; SiO₂ 0.43;
126 FeO 0.04; Na₂O 0.25; F 3.09; Cl 0.42; SO₃ 0.33.

127 We conducted two types of experiments ([Table 1](#)). The ‘dry’ experimental runs contained
128 90% SANK 1.3 gel, and equal amounts of two or three different apatite types ground together in
129 an agate mortar before loading into either 1 cm long, 3 mm wide Au capsules (low temperature
130 experiments) or Pt capsules (high temperature experiments), which were arc-welded shut. The
131 ‘wet’ experimental runs were identical to the ‘dry experiments’ except for containing an
132 additional 4 wt% H₂O ([Table 1](#)). The H₂O was loaded first before the solids. The Au or Pt
133 capsules were checked for leaks by weighing, heating in a 105 °C oven overnight, and then
134 weighed again. Any capsule that showed weight loss was discarded.

135 Trial experiments at natural granite magma conditions were first run in standard, cold
136 seal, 6 mm bore autoclaves on a hydrothermal line at 750 °C and 200 MPa for 2000 hours with
137 H₂O as the pressure medium. These experiments were buffered at approximately the Ni-NiO
138 oxygen buffer resulting from the presence of Ni metal filler rods, which occupied the bore of the
139 autoclave not occupied by the Pt capsules. Temperatures were measured externally by a
140 thermocouple tip inserted into the end of autoclave near the Pt capsules. Thermocouples are

141 accurate to within ± 3 °C. No variation in temperature was observed during each run. The
142 maximum temperature gradient along the length of a capsule was approximately 5 °C. Pressure
143 on the hydrothermal line was calibrated against a pressure transducer calibrated against a Heise
144 gauge manometer for which the quoted pressure is accurate to ± 5 MPa. The autoclaves were
145 quenched after the run using compressed air, reaching temperatures of ca. 100 °C within 1
146 minute.

147 These experiments produced little or no detectable physical or chemical changes in the
148 apatite compositions. After some further trials, experiments at 1200 °C, 200 MPa, 192 h were
149 run in an internally heated gas pressure vessel (IHPV) at the GeoForschungsZentrum (GFZ) in
150 Potsdam, Germany. The two advantages of these run conditions are that apatite is the only solid
151 phase, and that physical-chemical equilibration is still only partial. The IHPV used is a Harwood
152 argon-pressurized vessel at the GeoForschungsZentrum (GFZ) in Potsdam, Germany, which can
153 reach a maximum pressure and temperature of 1 GPa and 1250 °C, respectively. [Holloway](#)
154 [\(1971\)](#) and [Berndt et al. \(2002\)](#) provided general descriptions of IHPVs and rapid quench sample
155 holder setups. The pressure vessel consists of several components: an autoclave, an intensifier, a
156 pre-pressure pump, and an electrical switchboard. The GFZ autoclave is a tool-steel cylinder
157 surrounded by H₂O-cooled copper-tube windings, where a resistance furnace together with a
158 sample holder is inserted from the bottom and fixed onto a closure head sealing the vessel. The
159 thermal gradient inside the sample holder is controlled by two internal S-type (Pt-Pt90Rh10)
160 thermocouples connected to two separate heating loops (molybdenum wires), which are hooked
161 up to a EUROTHERM program controller. Temperature variations along the length of the
162 capsules are less than 5 °C. Pressure is measured *in-situ* with a pressure gauge (measurement

163 accuracy: 1 MPa), while pressure variations were less than 5 MPa, being automatically adjusted
164 throughout the experimental run duration.

165 Experimental run-conditions were kept constant at 1200 °C and 200 MPa for 192 h
166 utilizing two middle thermocouples in contact with the samples (**Table 1**). Each run consisted of
167 a Pt basket suspended by a Pt wire holding up to six Pt capsules (maximum length 30 mm).
168 Isobaric, rapid quench (~150 °C/sec) was achieved by melting the Pt wire such that the Pt basket
169 dropped into the lower ceramic falling tube part of the sample holder which was kept at room
170 temperature ([Berndt et al., 2002](#)).

171 After quench, the capsules were extracted, carefully examined, cleaned, weighed, and
172 opened. The capsules were then dried at 105 °C overnight. A portion of the extracted experiment
173 was mounted in epoxy and polished for back scattered electron (BSE) imaging and electron
174 microprobe (EMP) analysis.

175

176 **Scanning electron microscope observation**

177 The backscattered electron (BSE) images and preliminary chemical analyses were
178 performed on TESCAN Mira3 LMU field emission scanning electron microscope (FE-SEM) at
179 St. Mary's University. It is equipped with an Oxford Instrument X-Max 80 mm² large-area
180 silicon drift detector energy-dispersive X-ray spectrometer. Operating conditions were 20 kV
181 with an electron beam spot size of about 5 nm.

182

183 **Electron microprobe (EMP) analysis**

184 Chemical analyses of apatite crystals were performed using the JEOL Hyperprobe JXA-
185 8500F and 8530F+ microprobes at GFZ Potsdam with five wavelength dispersive spectrometers.
186 The samples were coated with a 20 nm thick carbon film and analysed for major and trace
187 elements using an accelerating voltage of 15 kV and a spot size of 10 μm . Standards and
188 operating conditions for EMP analysis of the three apatite types and the peraluminous granite
189 glasses are contained in [Tables 2](#) and [3](#), respectively. To increase the count statistics for trace
190 elements, but minimize volatile (F, Cl) diffusion ([Stormer et al., 1993](#); [Goldoff et al., 2012](#)), a
191 current of 20 nA was applied. Volatiles were measured first.

192 Problems in measurement of F in apatite grains include: (i) count rates are low for low
193 atomic number elements; (ii) concentrations of F are low (maximum F = 3.77 wt% in
194 fluorapatite); (iii) volatilization of F can occur under the electron beam, resulting in decreasing
195 count rates with time; (iv) the count rate on F, and thus apparent concentration of F, varies as a
196 function of the orientation of the apatite grain ([Stock et al., 2015](#); [Stormer et al., 1993](#); [Wudarska](#)
197 [et al., 2021](#)); and (v) secondary fluorescence effects. Because of these problems, the error bars
198 for F are large, and we report only the means in the subsequent tables and figures. This error in F
199 measurement translates over to the estimation of OH on the halogen site for an assumed apatite
200 formula of $\text{Ca}_5(\text{PO}_4)_3(\text{F,Cl,OH})$, because it is a calculated value based on the assumption that the
201 halogen site is fully occupied by F, Cl, and OH, and that the total charge on the halogen site is -1.

202 For quantitative chemical analyses of the peraluminous granite glasses, a 15 kV, 20 nA,
203 20 μm diameter electron beam was applied to achieve an acceptable current density of 0.06
204 nA/mm^2 ([Morgan and London, 2005](#)). Under such conditions, the Na loss could be 5%, which is
205 on average 0.18 wt% Na_2O . Further specifications regarding the calibration material and

206 counting times are given in **Table 3**. Volatiles such as F and Na were measured first, using the L-
207 type variants of necessary crystals to achieve the maximum count rate within the shortest
208 measurement time. Although peaks are narrow, L-type crystals show much higher counting rates
209 than former J-type crystals and are therefore more suitable for trace element concentrations.
210 Minimum detection limits at 3-sigma above mean background are in the range of 0.01 to 0.06
211 wt% for all analysed elements except for REE₂O₃ (0.09 wt%) and F (0.12 wt%).

212 Qualitative line scans were done using the JXA 8500F with 15kV and 5nA. For grains larger
213 than 10 µm the stage scan was used. For smaller grains the beam scan was used. Dwell times
214 varied from 0.5-2s and probe size from ~0.5 to 1µm.

215 **Laser ablation inductively coupled plasma mass spectrometry (LA-ICP-MS)**

216 Trace-element concentrations in the Durango apatite starting material and run-product
217 glasses were determined using the laser ablation inductively coupled plasma mass spectrometry
218 (LA-ICP-MS) facility located in the Health and Environments Research Centre (HERC)
219 Laboratory at Dalhousie University. The system employs a frequency quintupled Nd:YAG laser
220 operating at 213 nm, coupled to a Thermo Scientific iCAP Q ICPMS quadrupole mass
221 spectrometer with He flushing the ablation cell to enhance sensitivity ([Eggins et al., 1998a,b](#)).
222 Samples were analysed using a laser repetition rate of 10 Hz, spot size of 25 µm, and laser output
223 of ~5 J/cm². All samples were analysed by rastering the beam across the sample surface. Factory
224 supplied time resolved software (Qtegra) was utilized for the acquisition of individual analyses.
225 A typical analysis involved 20 seconds of background acquisition with the ablation cell being
226 flushed with He, followed by laser ablation for 60 seconds, then 40 to 60 seconds of cell
227 washout. Analyses were collected in a sequence in which two analyses were done on the NIST
228 610 standard reference material at the start of the acquisition cycle, then after every 20 analyses

229 on the unknowns. All LA-ICP-MS data reduction was done off-line using the Iolite version 4.0
230 software package (Paton et al., 2011). Ablation yields were corrected by referencing to the
231 EPMA-measured concentration of Ca in the apatite and the glass.

232

233 **RESULTS AND DISCUSSION**

234 In this section, we present the results, and discuss, sequentially, all our observations on
235 the chemical compositions of the run-product apatite grains, the glass compositions, the diffusion
236 rates, the textural appearance of the run-product apatite grains, and an example of apatite
237 contamination from the South Mountain Batholith. In our analysis of the results, we consider
238 only stoichiometric $\text{Ca}_5(\text{PO}_4)_3(\text{F},\text{Cl},\text{OH})$, with no consideration of a possible oxyapatite
239 component.

240

241 **Chemical Composition of Run-Product Apatite Grains**

242 **Preliminary experiments at 750 °C, 200 MPa, and 2000 h.** To determine the rate of chemical
243 and textural equilibration of the fluorapatite and Durango apatite in a peraluminous granitic melt,
244 a set of experiments containing these two apatites plus SANK 1.3 gel experiments plus water
245 were first conducted at geologically reasonable operating conditions, i.e., 750 °C, 200 MPa, and
246 2000 h. Both of the starting apatite compositions showed little textural change, except for slight
247 rounding of the corners of the shards. The Durango fluorapatite appears to show some evidence
248 of diffusion of Cl out of the solid grain with presumably some exactly reciprocal diffusion of OH
249 into the apatite grain (Figure 1).

250 After a set of additional experiments at 1000 °C, 200 MPa, and 72 h, in the IHPV, utilizing Pt
251 capsules, produced results similar to the 750 °C experiments, we then decided to run the
252 experiments at 1200 °C, 200 MPa, and 192 h as a final attempt to obtain an approach to chemical
253 equilibrium between some of the components in the melt and apatites, as well as an approach to
254 textural equilibrium.

255

256 **Experiments at 1200 °C, 200 MPa, and 192 h with two starting apatite compositions.** Here
257 the two starting apatites consisted of the three possible pairs of synthetic fluorapatite (F-Ap),
258 synthetic chlorapatite (Cl-Ap), and natural Durango apatite (D-Ap) ([Table 1](#)). The principal
259 chemical differences between the apatite starting materials are in the halogens and the REEs. The
260 starting synthetic fluorapatite has 3.77 wt% F, but no Cl or REEs; the starting synthetic
261 chlorapatite has 6.81 wt% Cl, but no F or REEs; and our measured starting Durango apatite has
262 means of 3.39 wt% F, 0.43 wt% Cl, and 0.91 wt% Σ REEs ($\text{La}_2\text{O}_3 + \text{Ce}_2\text{O}_3$). [Table 4](#) shows the
263 mean halogen compositions for the apatite run products in the six experimental runs, including
264 the starting compositions. [Figure 2](#) shows a mol proportion F-Cl plot of those apatite grains. The
265 composition of the run product apatite should be the average of the two starting material apatites,
266 minus the amounts of F and Cl variously taken up in the melt and separate fluid phase (if
267 present).

268 Run-product apatite grains in AA-11 and AA-14 have low F/Cl, as in the Cl-Ap + D-Ap
269 starting material ([Table 4](#)). Run-product apatite grains in AA-10 and AA-13 have high F/Cl, as in
270 the F-Ap + D-Ap starting material. Run-product apatite grains in AA-9 and AA-12 have
271 inexplicably high F/Cl, unrelated to the F-Ap + Cl-Ap starting material. The only difference is

272 the absence of Durango apatite and REEs. The question then arises as to whether the REEs
273 somehow stabilize the F/Cl ratio in the run products.

274 Calculating by difference from [Figure 2](#), apatite grains in the AA-9 ‘dry’ run have 13
275 mol% OH, whereas those in the AA-12 ‘wet’ run have 19 mol% OH, an increase of 1.46 times.
276 Similarly, apatite grains in the AA-10 ‘dry’ run have 9 mol% OH, whereas those in the AA-12
277 ‘wet’ run have 16 mol% OH, an increase of 1.78 times. Finally, apatite grains in the AA-11 ‘dry’
278 run have 24 mol% OH, whereas those in the AA-14 ‘wet’ run have 46 mol% OH, an increase of
279 1.91 times. Apparently, the higher the concentration of Cl in the starting materials, the greater is
280 the loss and replacement by OH ([Kusebauch et al., 2015](#)).

281 Only runs AA-10, AA-11, AA-13, and AA-14 contain the Durango apatite, and therefore
282 REEs, in the starting materials ([Table 1](#)). If the run-product apatite grains had reached
283 equilibrium for the rare-earth elements, their compositions should be the average of the two
284 starting material apatites, minus the (minor) amounts of La_2O_3 and Ce_2O_3 taken up in the melt.
285 [Figure 3](#) shows that the ΣREE contents in the run-product apatites span the entire range from the
286 Durango apatite to each of the synthetic apatites, suggesting that the system had not yet reached
287 chemical equilibrium for ΣREEs at these run conditions. Instead, the spread in ΣREE
288 concentrations in the run-product apatite grains is a combination of Durango losing ΣREE and
289 the synthetic fluorapatite or chlorapatite gaining ΣREE , but in no case has the system reached
290 chemical equilibrium for the ΣREEs .

291

292

293 **Experiments at 1200 °C, 200 MPa, and 192 h with three starting apatite compositions.** Runs
294 AA-15 to AA-18 contain all three apatites (synthetic fluorapatite, synthetic chlorapatite, natural
295 Durango apatite) as starting materials (**Table 1**). As in the experiments with two apatite starting
296 materials, the ratio of apatite/(apatite + SANK 1.3) = 0.10. **Table 5** shows the mean halogen
297 compositions for the apatite run products, and **Figure 4** shows a mol proportion F-Cl plot of these
298 grains. As above, the composition of the run-product apatite grains should be the average of the
299 three starting material apatites, minus the amounts of F and Cl taken up in the melt and separate
300 fluid phase (if present).

301 Unlike the runs containing two apatite compositions, the presence of Durango apatite in
302 these four runs does not appear to stabilize F/Cl in the starting materials and run products. The
303 ‘dry’ runs (AA-15, AA-17) have a low (OH) component; the ‘wet’ runs (AA-16, AA-18) have a
304 high (OH) content, but the run apatite grains in these experiments did not acquire as much (OH)
305 as in the two-apatite experiments.

306 As in the runs with two apatite starting compositions, if the run-product apatite had
307 reached equilibrium for the REE, their compositions should be the average of the three starting
308 material apatites, minus the (minor) amount of La_2O_3 and Ce_2O_3 taken up in the melt and
309 separate fluid phase (if present). **Figure 5** shows that the ΣREE ($\text{La}_2\text{O}_3 + \text{Ce}_2\text{O}_3$) contents in the
310 run-product apatites span almost the entire range from the Durango apatite to each of the
311 synthetic apatites, suggesting again that the system had not reached chemical equilibrium for
312 ΣREEs at the chosen run conditions. Also, relative to the results involving two-apatite starting
313 compositions, the compositions of analysed grains in the three-apatite runs are skewed towards
314 low concentration of REEs. This skewness possibly reflects a combination of the 2:1 ratio of

315 REE-free to REE-bearing apatite in the starting materials and the coarser grain sizes in runs AA-
316 17 and AA-18 that inhibit equilibration by chemical diffusion.

317

318 **Chemical composition of run-product glasses**

319 [London et al. \(2012\)](#) cautioned that finely-ground starting materials absorb atmospheric
320 H₂O onto their surfaces, and that it remains there under desiccation. The starting SANK 1.3 gel,
321 was kept dry in a drying oven at 105 °C. However, in an experiment where a sample of the gel
322 was placed in a crimped platinum capsule and heated it to 1000°C for 2 hours, the weight loss
323 was 3.6%. Thus, the starting material for the ‘dry’ runs may contain approximately 4% H₂O, and
324 the starting material for the ‘wet’ runs, with 4% added H₂O, may contain approximately 8%
325 H₂O. To facilitate comparison of the compositions of the glasses, we report their compositions as
326 anhydrous ([Table 6](#)).

327

328 **Major Elements in Runs AA-9 and AA-12.** Runs AA-9 and AA-12 contained F-Ap and Cl-Ap
329 and were ‘dry’ and ‘wet’, respectively. Glass AA-9 contained some small bubbles, whereas glass
330 AA-12 contained many larger bubbles ([Figure 6](#)); thus, both melts appear to have been saturated
331 with H₂O vapor.

332 [Table 6](#) reports the compositions of the starting gel and the glasses in runs AA-9 and AA-
333 12. The starting gel, SANK 1.3, contains no components other than SiO₂-Al₂O₃-Na₂O-K₂O. Any
334 other component in the run glasses has come from dissolution of apatite, namely CaO, P₂O₅, F
335 and Cl; however, the concentration of F is below the EMP lower limit of detection, because it
336 has been strongly partitioned into apatite ([Webster et al., 2009](#); [Li and Hermann, 2017](#)). Also, the

337 REEs are absent because there was no Durango apatite in the starting materials. There are several
338 implications arising from the compositions of the glasses in runs AA-9 and AA-12.

339 First, the CaO/P₂O₅ wt% ratio in stoichiometric apatite is 1.34, but this ratio is 2.47 ±
340 0.10 in the ‘dry’ AA-9 glass and 3.36 ± 0.15 in the ‘wet’ AA-12 glass. If apatite had simply
341 dissolved congruently in the SANK 1.3 melt, the CaO/P₂O₅ ratio in the glass should be 1.34.
342 Alternatively, if the apatite had dissolved incongruently, there should be a new solid phase in the
343 run products (e.g., [Wolf and London 1995](#)), but apatite is the only solid present. The remaining
344 explanation for the ‘missing’ P₂O₅ is that it partitioned into the fluid as either H₃PO₄ or as one or
345 more sodium phosphate complexes ([London et al., 1993](#); [Keppler, 1994](#)). For run AA-12, which
346 contains more water, these additional fluids could have extracted more P₂O₅ from the glass
347 (resulting in a higher CaO/P₂O₅ ratio in the glass) than in run AA-9. Assuming that, in our
348 experiments, CaO is a more reliable indicator of apatite solubility than P₂O₅, we can use our
349 measured CaO and P₂O₅ _{meas} concentrations in the glasses to calculate adjusted values of P₂O₅ _{adj}
350 (Table 6) so that the CaO/P₂O₅ ratio in the glass is also 1.34.

351 Second, except for the appearance of the dissolved apatite components, the glass
352 compositions in the two runs are similar to that of the starting gel (Table 6); however, the
353 peraluminosity (A/CNK) is significantly different. Clearly, apatite dissolution has introduced
354 CaO into the melt and has lowered its A/CNK from an initial value of 1.3 to ≈ 1.0.

355 Solubility of apatite is always expressed in terms of some function of P₂O₅ content. We
356 can compare our apatite solubility data, as indicated by P₂O₅ _{meas} or P₂O₅ _{adj}, at 1200 °C, 200
357 MPa, and 75% SiO₂, with other determinations, as follows:

358 (a) No agreement with the dependence of apatite solubility, as determined by P_2O_5 in the melt,
359 on peraluminosity using the empirical relationship

$$360 \quad P_2O_{5\text{melt}} = -3.4 + 3.1*(A/CNK)_{\text{melt}} \quad (1)$$

361 of [Wolf and London \(1994\)](#). However, their experiments were done at the much lower
362 temperature of 750 °C, and apatite solubility is strongly dependent on temperature ([Harrison and](#)
363 [Watson 1984](#)).

364 (b) Potential agreement with the dependence of apatite solubility on peraluminosity, as
365 determined by P_2O_5 in the melt ([Pichavant et al. 1992; Fig. 2](#)), but requiring an extrapolation
366 well beyond their experiments at 1000 °C.

367 (c) Good fit with the dependence of the apatite solubility parameter, as determined by
368 $\ln((P_2O_5)^{1.5}*(CaO)^5)$, on melt SiO_2 [$P_2O_5_{\text{meas}} = 2.40$ and $P_2O_5_{\text{adj}} = 3.66$ are within the range
369 reported by [Tollari et al. \(2006; Fig. 10\)](#) for 80.57 and 82.40 mol% SiO_2 , respectively].

370 (d) Reasonable fit with the dependence of apatite solubility on melt SiO_2 , as determined by
371 $\ln D_P^{\text{apatite/melt}}$ [= 4.2 for $P_2O_5_{\text{meas}}$ and 3.4 $P_2O_5_{\text{adj}}$ compared with 4.0 for ([Harrison and Watson](#)
372 [1984; Fig. 3](#)) at 1200°C.

373 (e) Better fit for mean $P_2O_5_{\text{meas}}$ (0.66 wt %) than for mean $P_2O_5_{\text{adj}}$ (1.40 wt %) for the
374 dependence of apatite solubility on temperature ([Green and Watson \(1982; Fig. 2\)](#), who report
375 P_2O_5 concentrations of 0.5 to 1.0 wt % in melts with 75 wt% SiO_2 at temperatures between 1080
376 and 1165 °C.

377 In summary, given the differences in temperature-pressure-composition conditions, the solubility
378 of apatite in our experiments is broadly compatible with a wide range of previous work.

379 Third, the concentration of CaO in the ‘wet’ glass of AA-12 is slightly higher than in the
380 ‘dry’ glass of AA-9 (Table 6), suggesting that H₂O might have some positive effect on apatite
381 solubility.

382 Fourth, in our experiments, the starting melt has A/CNK=1.3, but as apatite begins to
383 dissolve, the A/CNK of the melt decreases, and apatite solubility contrarily decreases (Wolf and
384 London 1994; Pichavant et al. 1992). Ultimately, apatite dissolution stops because the melt
385 becomes saturated. In our runs, the apatite grains stopped dissolving when the A/CNK of the
386 melt reached approximately 1.0 (i.e., neither peraluminous nor metaluminous). Further
387 dissolution of apatite would take the composition of the melt into the metaluminous (A/CNK <
388 1) domain where apatite solubilities are less well documented.

389 Fifth, our experimental run products consist solely of apatite + glass ± vapor ± saline
390 fluid. The concentration of Cl in the ‘dry’ and ‘wet’ glasses is identical, meaning that
391 equilibrium had been reached between the melt and apatite, regardless of the existence or
392 proportion of a separate fluid phase. From Tables 4 and 6, the apatite in ‘dry’ run AA-9 has 1.34
393 ± 0.04 wt% Cl and the glass has 0.21 ± 0.01 wt% Cl. The apatite in ‘wet’ run AA-12 has 0.59 ±
394 0.05 wt% Cl and the glass has 0.21 ± 0.01 wt% Cl. Thus, in the ‘dry’ run, AA-9, the average
395 $Cl_{ap}/Cl_{gl} = 6.38 \pm 0.36$, i.e., Cl is strongly partitioned into the apatite and the minor fluid phase.
396 In the ‘wet’ run, AA-12, the average $Cl_{ap}/Cl_{gl} = 2.81 \pm 0.27$, i.e., Cl is less strongly partitioned
397 into the apatite, presumably preferring the more abundant free fluid phase, and OH must replace
398 the Cl leaving the apatite. As evidence of the partitioning of Cl into the fluid phase, small
399 crystals of NaCl occur in some of the bubbles in the glasses.

400 Finally, Webster (1992, Fig. 5) and Webster et al. (2015) used the concentration of Cl in
401 haplogranitic melts to estimate the concentration of Cl in coexisting fluid phases. By this simple
402 metric, our glasses with 0.21 wt% Cl would coexist with a fluid containing ~10 wt% Cl.

403 Alternatively, Webster and Piccoli (2015, Fig. 4) used the partitioning of Cl between apatite and
404 glass to infer the concentration of Cl in a coexisting aqueous fluid phase. By this more complex
405 metric, the fluid phase in ‘dry’ run AA-9 should have contained ~68 wt% Cl, and the coexisting
406 fluid in ‘wet’ run AA-12 should have contained ~23 wt% Cl. Given these uncertainties in the Cl
407 concentration in the fluids, and the unknown proportions of the run products (apatite-glass-fluid),
408 calculating a mass balance for Cl between starting materials and run products is not possible.

409 **Rare-Earth Elements in Runs AA-10 and AA-13.** Runs AA-10 and AA-13 contained synthetic
410 fluorapatite and natural Durango apatite and were ‘dry’ and ‘wet’, respectively. As above, the
411 starting granite gel contained only SiO₂-Al₂O₃-Na₂O-K₂O, so all other elements must have come
412 from the dissolution of apatite, including REEs from the Durango apatite. Table 7 shows the
413 concentrations of the REEs in the glasses and the Durango apatite. The first generalization is that
414 the concentrations of REEs in the ‘dry’ AA-10 glass and ‘wet’ AA-13 glass are very similar,
415 suggesting that system H₂O content, at least for concentrations under 10%, is not important in
416 the dissolution of these trace elements. The second generalization is that, for the REEs, the
417 homogeneous glasses contain about 1% of the REE concentrations present in the heterogeneous
418 Durango apatite.

419 **Modeling diffusive re-equilibration of Cl and REE**

420 Measured elemental abundances in apatite from the series of experiments done at 1200
421 °C for 192 hours reveal generally homogeneous levels of Cl, but a significant range for the REE
422 (i.e., Figures 3 and 5). The exception to this homogeneity is the variation in Cl concentrations in

423 apatite from experiment AA-17 (and to a lesser extent AA-18), which show a level of variation
424 of up to 30%, exceeding the typical analytical uncertainty of <10%. In each experiment, large
425 compositional gradients in Cl and the REEs were induced using apatite starting materials that
426 have initial concentration levels that are higher or lower than equilibrium values. Whereas
427 wholesale dissolution and reprecipitation would serve to homogenize both the halogens and REE
428 (which likely occurred on a limited scale as evidenced by crystal faceting), differences in the
429 volume diffusion properties of these elements could result in the variable degrees of
430 homogeneity. As summarized by [Cherniak \(2010\)](#), diffusion coefficients in apatite for the
431 anions (OH, F, Cl and O) all show directional anisotropy (faster parallel to c) and are 1-3 orders
432 of magnitude more rapid than the fastest diffusion trace element cations (Sr and Pb) at geological
433 temperatures. In contrast to the cation sites, the anion columns in apatite therefore represent
434 highly directional, rapid transport pathways through the apatite structure.

435 [Cherniak \(2000\)](#) documented several diffusion mechanisms for the REE in apatite,
436 depending on the substitution mechanism involved. Diffusion coefficients are similar to other
437 divalent cations if simple isovalent REE exchange is involved (e.g., Ce diffusion into apatite that
438 already contains Ce and other LREEs), but more than 10 times slower if a coupled exchange of
439 either $\text{REE}^{+3} + \text{Si}^{+4} \rightarrow \text{Ca}^{+2} + \text{P}^{+5}$ or $\text{REE}^{+3} + \text{Na}^{+1} \rightarrow 2\text{Ca}^{+2}$ is involved to maintain charge
440 balance in the lattice ([Pan and Fleet, 2002](#)). Thus, if the REE move by solid state diffusion in the
441 lattice they must couple with a Na or a Si ion as well. This constraint dramatically reduces the
442 diffusion rate, even at high temperatures (cf. [Cherniak, 2010](#)). The most efficient means by
443 which REE can be moved in or out of the apatite would be via a coupled dissolution-
444 reprecipitation process where REE movement would be facilitated by fluids in an interconnected
445 porosity in the metasomatized areas of the apatite and the possible formation of monazite

446 inclusions or rim grains (see [Harlov et al., 2002, 2005](#); [Harlov and Förster, 2003](#)). Such a
447 dissolution-reprecipitation process was apparently not the case here because no apatites from the
448 experiments show metasomatized textures nor the formation of monazite inclusions or rim
449 grains. Instead, the granitic melt interacted with the apatite in such a manner that promoted the
450 exchange of REE between the melt and apatite, based solely on solid state diffusion of REE in
451 the apatite and REE diffusion in the melt. This deduction indicates that the granitic melt was not
452 chemically reactive with either the fluorapatite (synthetic or Durango) or chlorapatite. Rather,
453 each of the three apatite types experienced only some dissolution in, and partial recrystallization
454 from, the melt.

455 To test the hypothesis that highly variable diffusion rates explain the differences in
456 halogen and REE equilibration in the apatite grains, we calculated model diffusion profiles to
457 simulate re-equilibration of spherical apatite grains using halogen and REE diffusion parameters
458 reported in previous studies ([Table 8](#)). The choice of a spherical grain model is a simplification,
459 but given the wide variability in the shape of grains introduced as powders ([Figures 1, 8, and 9](#)),
460 it serves as a useful approximation for a radial diffusive flux. The solution to Fick's Second law
461 for diffusion into a sphere of radius, a , having an initial solute concentration, C_i , and a
462 concentration at $r = a$ (the crystal-melt interface) fixed at C_o is ([Crank, 1975](#); equation 6.18):

463
$$\frac{C-C_i}{C_o-C_i} = 1 + \frac{2a}{\pi r} \sum_{n=1}^{\infty} \frac{(-1)^n}{n} \sin \frac{n\pi r}{a} \exp\left(-\frac{Dn^2\pi^2 t}{a^2}\right) \quad (2)$$

464 where D is the diffusion coefficient in m^2/second , t is time in seconds, and r is the radial distance
465 ($r = 0$ is the centre of the sphere, $r=a$ is the outer margin). With the corresponding solution at
466 short times as ([Crank, 1975](#); equation 6.21):

467
$$\frac{C-C_l}{C_o-C_l} = \frac{a}{r} \sum_{n=0}^{\infty} \left\{ \operatorname{erfc} \frac{(2n+1)a-r}{2\sqrt{(Dt)}} - \operatorname{erfc} \frac{(2n+1)a+r}{2\sqrt{(Dt)}} \right\} \quad (3)$$

468 in which erfc is 1-erf, and erf is the error function. Values of the diffusion coefficient at a
469 particular temperature were calculated using the Arrhenius equation:

470
$$D = D_o \exp(-E_a/RT) \quad (4)$$

471 in which D_o is the pre-exponential factor (m^2/s), E_a is the activation energy (kJ/mol), and R is the
472 gas constant (J/K/mol). Each of the apatite re-equilibration experiments involved apatite starting
473 materials having different initial concentrations of the halogens and REE, in turn imposing
474 differences in C_l . Values of C_o are dictated by the equilibrium apatite/melt partition coefficient
475 and would, therefore, be the same for each apatite grain, regardless of the initial internal
476 composition. The direction of the diffusive flux is variable as well; Cl will diffuse out and F
477 diffuse in for the Cl-apatite starting material, with the opposite sense for the F-apatite starting
478 material. In terms of the REE, both Cl-apatite and F-apatite are REE-free, requiring uptake of
479 REEs to approach equilibrium. The situation is less clear for the Durango apatite starting
480 material, which contains elevated, but somewhat variable levels of the REE (~0.6 to 1.7 wt%
481 $\text{La}_2\text{O}_3+\text{Ce}_2\text{O}_3$; [Figure 5](#)). A value for the equilibrium C_o for the REE can be estimated using the
482 apatite/melt partitioning data of [Watson and Green \(1981\)](#) who measured $D_{\text{Sm}}^{\text{apatite/melt}}$, the
483 apatite/melt partition coefficient for Sm, as a function of the melt SiO_2 concentration, yielding an
484 interpolated value of ~15 at the SiO_2 concentration of the melt used in this study. The REE
485 content of the melts from experiments AA-10 and AA-13, both containing Durango apatite, is
486 ~0.013 wt% $\text{La}_2\text{O}_3+\text{Ce}_2\text{O}_3$, yielding an equilibrium C_o of ~0.20 wt% for those experiments.
487 Other experiments with Durango apatite are assumed to have similar levels of REE in the melt,
488 and therefore C_o . Estimating values of C_o for the halogens is complicated by differences in the

489 proportions of the different apatite types, as well as melt water content, and the fact that apatite-
490 melt partitioning cannot be modeled by a simple Nernst-type partition coefficient, but instead
491 requires the full mass balance involving F-OH, Cl-OH and Cl-F exchange (e.g. [McCubbin et al.](#)
492 [2015](#); [Li and Costa 2020](#); [Piccoli and Candela, 1992](#); [Webster et al., 2017](#)). Alternatively, a
493 value of C_0 can be estimated by the concentration of the halogens in the run-product apatites, as
494 their homogeneity likely represents melt-crystal equilibrium achieved over the entire grain-scale,
495 an assumption that is borne out by the diffusion models.

496 Model diffusion profiles for Cl at 1200 °C used the diffusion parameters for F-OH-Cl
497 exchange reported by [Brenan \(1994\)](#); listed in [Table 8](#)) for diffusion parallel to the c-axis. [Brenan](#)
498 [\(1994\)](#) also report diffusion coefficients measured parallel to the a-axis that are ~100 times
499 slower, therefore the predominant diffusive flux for re-equilibration will be along the c-axis
500 (anisotropy in the diffusion of the REE has not, to our knowledge, been measured or reported
501 [\(Cherniak, 2010\)](#)). Diffusion profiles are calculated for durations of 2, 10, and 50 hours, thus less
502 than the 192 hour run-times of the experiments. The profiles presented in [Figure 7a](#) were
503 calculated with equation 2. The model simulates diffusion in a 50 μm radius grain of Durango
504 apatite with a value for C_1 of 0.43 wt% Cl (average reported in [Table 4](#)), with C_0 pinned at the
505 value corresponding to experiment AA-14 (concentrations from other experiments would yield
506 the same overall result in terms of extent of equilibration). As is clear from [Figure 7a](#), complete
507 homogenization of the grain at 1200 °C is essentially complete after 50 hours. For this grain
508 size, employing the diffusion coefficient for Cl measured by [Li et al \(2020\)](#) would yield a similar
509 result, but requiring 100 hours for complete homogenization. The Cl diffusivity reported in [Li et](#)
510 [al. \(2020\)](#) corresponds to a “tracer diffusivity”, meaning that it applies to diffusion in the absence
511 of OH or F counter fluxes and is, therefore, expected to be larger than the value applicable to F-

512 Cl-OH apatite solutions, thus the re-equilibration time modeled using the [Li et al \(2020\)](#) data is
513 probably a minimum time. Inspection of [Figures 1, 8, and 9](#) show that most apatite grain sizes
514 are generally less than 50 μm , indicating that an experiment duration of 192 hours at 1200 $^{\circ}\text{C}$ is
515 sufficient to completely homogenize the initial gradients in halogen concentration, consistent
516 with the experimental results. However, some larger ($> 100 \mu\text{m}$) grains are also evident, as
517 shown in [Figure 9](#) for experiment AA-17. Diffusion model results for grains with radii greater
518 than 150 μm indicate homogenization timescales of more than 200 hours. Therefore, analysis of
519 the central portions of these larger grains, such as in AA-17, would yield Cl concentrations either
520 above or below the equilibrium concentration, depending on the identity of the original apatite
521 precursor.

522 Model curves for the diffusive loss of the REE simulated for a grain of assumed Durango
523 apatite initial composition are shown in [Figure 7b](#). In this case, equation 2 is unstable for such
524 small values of the diffusion coefficient for the durations considered, and equation 3 was
525 employed instead. Unlike the case for Cl, the diffusion profiles for the REE show only limited
526 penetration into the apatite grain, extending to only $\sim 3 \mu\text{m}$ after 200 hours. Random microprobe
527 analyses of initial Durango apatite grains resulting from experiments subject to these conditions
528 would therefore yield total $\text{La}_2\text{O}_3 + \text{Ce}_2\text{O}_3$ concentrations ranging from C_1 (~ 0.6 to 1.7 wt%) to C_o
529 (~ 0.2 wt%). Cl-apatite and F-apatite grains that were initially REE-free would yield
530 concentrations ranging from a C_o of ~ 0.2 wt% to undetectable. This range of concentrations is
531 indeed observed in the analyses of run-product apatite, consistent with the limited extent of
532 diffusive re-equilibration predicted by the diffusion model. We conclude that the large
533 difference in the level of homogeneity exhibited by Cl and the REE is a product of diffusion-
534 controlled re-equilibration.

535

536 **Textural Modifications of Run-Product Apatite Grains**

537 [Figure 8](#) shows the apatite grain sizes and shapes in each of the six runs containing two
538 starting apatite compositions. All grains began as angular shards, but after the runs, they are all
539 rounded, and some show development of crystal faces. Theoretically, from the standpoint of the
540 surface/volume ratio, the many small irregular apatite shards in the starting materials should be
541 the first to become rounded as they all dissolve in the silicate melt, or disappear entirely
542 depending on the grain size, until the melt is saturated with apatite. With longer run times, the
543 remaining apatite grains should gradually develop crystal faces until all the grains become
544 euhedral as a continuation of the Ostwald ripening effect. Measurement of the attainment of
545 textural equilibrium are only qualitative, nevertheless we can make some statements about the
546 progress in this direction based on the development of crystal faces.

547 [Figure 9](#) shows the apatite grain sizes and shapes in the four runs containing three starting
548 apatite compositions. The run-product apatite grains appear to retain more of their initial angular
549 shapes than in the two-apatite experiments above, and there are fewer grains developing crystal
550 faces. [Figure 10](#) shows a schematic representation of what these experiments have shown
551 regarding how chemical and textural equilibrium is approached in a granitic melt. The physical
552 appearances of the grains can be deceptive. Euhedral grains of apatite, and all other minerals, can
553 be purely magmatic, peritectic, or of overgrown xenocrystic in origin. The default origin for a
554 euhedral grain is magmatic, because we expect that a mineral growing unrestrictedly in a silicate
555 melt, especially an early-saturated phase such as apatite, would develop unimpeded crystal faces,
556 at least up to the point where crystals interfere with each other. Peritectic grains are particularly
557 problematic, because they appear to be magmatic (e.g., andalusite - [Clarke et al. \(2005\)](#));

558 cordierite - [Erdmann et al. \(2009\)](#); K-feldspar - [MacDonald and Clarke \(2017\)](#)), despite their
559 constituent chemical components being foreign. Some euhedral grains are suspect magmatic,
560 because they are not common minerals in granites (andalusite, cordierite), and others are
561 particularly deceptive because they are also common as purely magmatic phases (K-feldspar).
562 Furthermore, two adjacent euhedral grains of the same mineral in the same rock can have
563 completely different origins. Only some combination of physical and chemical parameters can
564 reveal the correct interpretation of their origins.

565

566 **A Natural Example of Apatite Assimilation**

567 **Apatite mineralogy and compositions**

568 [Jähkel \(2010\)](#) investigated phosphate mineral relations along both sides of the contact of
569 the contaminated, post-tectonic, peraluminous South Mountain Batholith ([MacDonald, 2001](#);
570 [MacDonald and Clarke, 2017](#)) with metasedimentary rocks of the Meguma Supergroup. One
571 granite sample (P7G3) contains a chain of apatite grains extending in both directions from a
572 small xenolith into the enclosing granite (sample P7G3, [Figures 11a,b,c](#)), representing a
573 microcosm of the contamination process discussed in this paper. In simple terms, this natural
574 sample contains two distinct types of apatite, analogous to our synthetic experiments. The apatite
575 grains in the xenolith are small and anhedral; the apatite grains in the granite are large and
576 subhedral to euhedral. In the same granite sample, remote from the xenolith, are many other
577 apatite grains ([Figure 11d](#)), and in the adjacent country rocks, apatite occurs as ultra-fine-grained
578 bands ([Figure 11e](#)). [Table 9](#) shows the chemical compositions for these apatite grains in granite
579 sample P7G3, and [Figure 12](#) shows chemical variation diagrams for Ce-Y and Fe-Mn.

580 **F-Cl Relations**

581 All apatite grains (**Table 10**), regardless of their occurrence in the xenolith or in the
582 granite, and regardless of whether core or rim, have identical halogen compositions, within
583 analytical error. These results suggest that the halogens have reached chemical equilibrium in
584 this contaminated granite. We can deduce from our trial experiments at 750 °C, 200 MPa, and
585 2000 h, where halogen equilibrium was not reached, that this P7G3 natural system, at ca. 750 °C
586 and 300 MPa, clearly must have taken much longer than 2000 h (~ 3 months) to achieve its
587 chemical equilibrium for F-Cl. Our diffusion modeling shows that, at 750 °C, it would take 80
588 years to homogenize Cl in a 50 µm radius apatite grain, and 6000 years in a 500 µm radius
589 apatite grain.

590

591 **Ce₂O₃-Y₂O₃ and FeO-MnO Relations**

592 In the P7G3 natural apatite system, the concentrations of La are below our EMP
593 analytical lower limit of detection, but the Ce and Y concentrations are measurable. Thus, we use
594 Ce-Y in the natural system as a proxy for comparing with the La-Ce results in the synthetic
595 system. Also, except for minor Fe and Mn in the Durango apatite, our synthetic system contained
596 no first transition series elements, but almost all natural systems do, so we can examine them as
597 well (**Figure 12**). We make the following observations:

598 (i) The apatite grains show an extremely wide range of concentrations of Ce₂O₃ (0.03–0.26
599 wt%), Y₂O₃ (0.05–0.39 wt%), FeO (0.05–0.81 wt%), and MnO (0.28–0.97 wt%) in a single thin
600 section; (ii) the green ellipses enclose the tight element distribution in the apatite cores (grains A-
601 4, A-5, A-6, A-7) in the xenolith; and (iii) every apatite grain is zoned, but the core-rim vectors
602 do not point to a single composition.

603

604 **Interpretation**

605 In general, accessory minerals (apatite, monazite, zircon, magnetite, ilmenite, rutile,
606 allanite, titanite) in granites contain a wealth of petrogenetic information about age, temperature,
607 F/Cl ratios in the melt and coexisting fluid (if any), contamination, magma differentiation and
608 evolution as captured in zoning, etc. ([Stokes et al., 2019](#); [Wolf and London, 1994](#); [Lux et al.,](#)
609 [2006](#); [Webster and Piccoli, 2015](#); [Kusebauch et al., 2015](#); [Wones, 1989](#); [Anderson, 1996](#);
610 [Hoshino et al., 2007](#); [Carruzzo et al., 2006](#); [Jung et al., 2000](#)). In addition, textural evidence
611 ([Clarke et al., 2021](#)), supported by experimental work ([Wolf and London, 1994](#)), shows that
612 apatite may saturate early in peraluminous granite magmas such as the South Mountain
613 Batholith. If so, under such conditions of high T and low crystallinity, these early-formed apatite
614 grains might be expected to be homogeneous in composition, but apparently this is not the case.

615 Granite sample P7G3 is contaminated, clearly containing xenoliths of country rock.
616 Locard's Principle applied to this sample, namely the exchange of materials after physical
617 contact, indicates that the dual processes of attaining chemical and textural equilibrium
618 (assimilation) were still under way when this assemblage of cognate and foreign materials
619 reached its thermodynamic solidus temperature ([Clarke, 2007](#)). All the apatite grains in P7G3
620 have equilibrated, i.e., assimilated, with respect to F and Cl, but not for Ce-Y or Fe-Mn in the
621 granite magma that crystallized this rock. The wide chemical variation for Ce-Y and Fe-Mn in all
622 the apatite grains indicates that the rates of cooling above, and perhaps also below, the solidus,
623 were too rapid to achieve chemical equilibrium by diffusion. Likewise, the textural assimilation
624 is, at best, only partial. We deduce that, on the centimeter scale of the thin section, and even on
625 the micrometer scale of the single grains, the apatite grains in granite sample P7G3 have

626 probably had more than the two obvious sources (foreign from the one visible xenolith, and
627 cognate from the granite magma), as observed in other granites ([Lux et al., 2006](#); [Sun et al.,](#)
628 [2021](#), and references therein).

629 It is possible that the streaks of ultra-fine-grained apatites in country rock sample P6C1
630 ([Figure 11e](#)) were the precursors for the coarsened apatite chain in granite sample P7G3.
631 Specifically, however, any apatite grain in the xenolith almost certainly has a metamorphic
632 origin, but any apatite grain in the granite can be purely magmatic or modified xenocrystic in
633 origin, and those xenocrysts may be different from those in the one xenolithic source observable
634 in granite sample P7G3. The physical and chemical processes that may have been operating in
635 granite sample P7G3 include:

- 636 (i) fractional crystallization, to explain some of Ce-Y and Fe-Mn zoning in single crystals,
637 however zoning directions are not uniform, suggesting additional disequilibrium processes such
638 as magma recharge, magma mixing, and a wide range of xenocrystic apatite compositions, all
639 recorded by the apatite grains;
- 640 (ii) local conditions, e.g. apatite is included in, or proximal to, biotite, and an ability to exchange
641 with nearby, but much rarer, monazite or xenotime;
- 642 (iii) Ostwald ripening, including dissolution of small grains and overgrowth on large grains, to
643 explain some of the cases of reverse zoning of Ce-Y and Fe-Mn, as well as the textural changes
644 in apatite from small and anhedral to large and euhedral; and
- 645 (iv) diffusion of F-Cl through the silicate melt, including melt along grain boundaries in the
646 small xenolith, and through all the solid apatite grains to achieve chemical equilibrium for the
647 halogens.

648 Because the halogens have reached chemical equilibrium in granite sample P7G3, we
649 deduce that the time the natural system remained active for F-Cl exchange was on the order of
650 the modeled 80-6000 years noted above. [Bea \(2010\)](#) showed that the cooling rates of batholiths
651 to their solidus temperatures are on the order of thousands to tens of thousands of years. The
652 implication would then be that, however long the natural system took to crystallize, in this case
653 of the South Mountain Batholith, it was insufficient to equilibrate Ce-Y, or even Fe-Mn between
654 the melt and the apatite.

655

656

IMPLICATIONS

657 Contrary to the elementary textbook tripartite classification of rocks, granites are not
658 strictly igneous rocks, but rather hybrids. Granted, their principal component was a siliceous
659 silicate melt, but that melt had been in contact with foreign rocks from the time of its ascent out
660 of the source region to the time of its emplacement. Those foreign components can variously join
661 the initial silicate melt as xenoliths, xenocrysts (including restites), peritectic grains, and melt.
662 The more physically and chemically anomalous the solid foreign material is to the magmatic
663 crystallization products, the easier it is to identify as foreign (e.g., staurolite). The more
664 physically and chemically similar the solid foreign material is to the magmatic crystallization
665 products, the harder it is to identify as foreign (e.g., quartz). Between these extremes are
666 minerals, such as our natural apatite grains in sample P7G3, that show attainment of chemical
667 equilibrium for F and Cl, but not for Fe, Mn, Ce, and Y, and only some indication of attainment
668 of textural equilibrium. Granitic rocks would be much less revealing about their origins if they
669 had always reached physical and chemical equilibrium. In such a scenario, there would be no

670 textural or chemical information preserved about the past histories of their constituent minerals.
671 Consequently, *every mineral grain* in a granite must be interrogated about its origin.

672 As our experiments on, and natural example of, apatite have shown, foreign material will
673 undergo various degrees of physical and chemical equilibration with cognate material. In the rare
674 event of perfect physical and chemical equilibration of cognate and foreign material, only whole-
675 rock geochemistry can detect the former contamination. Otherwise, physically and/or chemically
676 identifiable relics of contamination remain, and this must be the case for most granites.

677 For 50 years, traditional whole-rock geochemistry (majors, traces, isotopes) and
678 application of assimilation-fractional crystallization (AFC) models have reached a petrogenetic
679 limit, and new approaches are needed. Given that all granites are contaminated rocks, we
680 propose that future petrogenetic work should begin to focus instead on a minerals-based
681 quantitative estimate of contamination (QEC). Such work would begin with a detailed inventory
682 and characterization of the minerals in the country rocks to establish the physical and chemical
683 properties of the contaminants, and continue the same characterization in the minerals of the
684 granite. Then apply a range of discriminant techniques, ranging from simple histograms to
685 multivariate statistics, for each quantifiable physical and chemical parameter in minerals of the
686 granite and country rock to arrive at independent quantifiable estimates of contamination (QEC)
687 for each phase.

688 Much of the otherwise tedious data collection can be automated. For example, [Clarke et](#)
689 [al. \(2021\)](#) examined the spatial association of >15,000 accessory mineral grains in three granite
690 samples, except that limited study needs to go further to assess the cognate or foreign origin for
691 every grain in the granite sample to get a minimum estimate for the extent of contamination,

692 given that some foreign grains may have completely equilibrated by dissolution, melting, or
693 diffusive ion exchange (Clarke, 2007).

694 **ACKNOWLEDGEMENTS**

695 Barrie Clarke acknowledges the generous opportunity to conduct the experimental work at GFZ-
696 Potsdam as well as to utilize the analytical equipment. James Brenan acknowledges the support
697 of an NSERC Discovery Grant and a Research Tools and Instruments Grant to establish the LA-
698 ICP-MS facility at Dalhousie University. Anne Jähkel acknowledges the facilities of the EMP
699 laboratories at Dalhousie University with the assistance of Dan MacDonald, Potsdam University
700 with the assistance of Christina Günter, and GFZ-Potsdam. We extend our thanks to reviewers
701 Weiran Li and Ricardo Sallet for their perceptive recommendations for improving our
702 manuscript, and to Justin Filiberto for efficient editorial handling.

703

704

REFERENCES CITED

- 705 Anderson, J.L. (1996) Status of thermobarometry in granitic batholiths. Special Paper –
706 Geological Society of America, 315, 125-138.
- 707 Bea, F. (2010) Crystallization Dynamics of Granite Magma Chambers in the Absence of
708 Regional Stress: Multiphysics Modeling with Natural Examples. *Journal of Petrology*, 51 1541-
709 1569. doi:10.1093/petrology/egq028.
- 710 Berndt, J., Liebske, C., Holtz, F., Freise, M., Nowak, M., Ziegenbein, D., Hurkuck, W., and
711 Koepke, J. (2002) A combined rapid-quench and H₂-membrane setup for internally heated
712 pressure vessels: Description and application for water solubility in basaltic melts. *American*
713 *Mineralogist* 87, 1717-1726.
- 714 Brenan, J. (1994) Kinetics of fluorine, chlorine and hydroxyl exchange in fluorapatite. *Chemical*
715 *Geology* 110, 195-210.
- 716 Carruzzo, S., Clarke, D.B., Pelrine, K., and MacDonald, M.A. (2006) Texture, composition, and
717 origin of rutile in the South Mountain Batholith, Nova Scotia. *The Canadian Mineralogist* 44,
718 715-729.
- 719 Cherniak, D.J. (2000) Rare earth element diffusion in apatite. *Geochimica et Cosmochimica*
720 *Acta* 64, 3871–3885.
- 721 Cherniak, D.J. (2010) Diffusion in Accessory Minerals: Zircon, Titanite, Apatite, Monazite and
722 Xenotime. *Reviews in Mineralogy & Geochemistry* 72, 827-869.
- 723 Clarke, D.B. (2007) Assimilation of xenocrysts in granitic magmas; principles, processes,
724 proxies, and problems. *The Canadian Mineralogist* 45, 5-30.
- 725 Clarke, D.B. (2019) The origin of strongly peraluminous granites. *The Canadian Mineralogist*
726 57, 529-550.
- 727 Clarke, D.B., and Carruzzo, S. (2007) Assimilation of country-rock ilmenite and rutile in the
728 South Mountain Batholith, Nova Scotia, Canada. *The Canadian Mineralogist* 45, 31-42.

- 729 Clarke, D.B., Dorais, M., Barbarin, B., Barker, D., Cesare, B., Clarke, G., El Baghdadi, M.,
730 Erdmann, S., Foerster, H.-J., Gaeta, M., and others (2005) Occurrence and origin of andalusite in
731 peraluminous felsic igneous rocks. *Journal of Petrology* 46, 441-472.
- 732 Clarke, D.B., Erdmann, S., Samson, H., and Jamieson, R.A. (2009) Contamination of the South
733 Mountain Batholith by sulfides from the country rocks. *The Canadian Mineralogist* 47, 1159-
734 1176.
- 735 Clarke, D.B., Renno, A., Hamilton, D.C., Gilbricht, S., and Bachmann, K. (2021) The Spatial
736 Association of Accessory Minerals with Biotite in Granitic Rocks from the South Mountain
737 Batholith, Nova Scotia. *Geosphere* 18, 1–18. <https://doi.org/10.1130/GES02339.1>.
- 738 Crank J. (1975) *The Mathematics of Diffusion*, 2nd ed. Oxford.
- 739 Eggins, S.M., Kinsley, S.P.J., and Shelley, J.M.M. (1998a) Deposition and element fractionation
740 processes during atmospheric pressure laser sampling for analysis by ICPMS. *Applied Surface*
741 *Science* 127-120, 278-286.
- 742 Eggins, S.M., Rudnick, R L., and McDonough, W.F. (1998b) The composition of peridotites and
743 their minerals; a laser-ablation ICP-MS study. *Earth and Planetary Science Letters* 154, 53-71.
- 744 Erdmann, S., Clarke, D.B., and MacDonald, M.A. (2004) Origin of chemically zoned and
745 unzoned cordierites from the South Mountain and Musquodoboit batholiths, Nova Scotia.
746 *Special Paper - Geological Society of America* 389, 99-110.
- 747 Goldoff, B., Webster, J.D., and Harlov, D.E. (2012) Characterization of fluor-chlorapatites by
748 electron probe microanalysis with a focus on time-dependent intensity variation of halogens.
749 *American Mineralogist* 97, 1103-1115. DOI: http://dx.doi.org/10.2138/am.2012.3812_1103.
- 750 Hamilton, D.L., and Henderson, C.M.B. (1968) The preparation of silicate compositions by a
751 gelling method. *Mineralogical Magazine*, 36, 832-838.

- 752 Harlov, D.E., Förster, H.-J., and Nijland, T.G. (2002) Fluid-induced nucleation of REE-
753 phosphate minerals in apatite: Nature and experiment. Part I. Chlorapatite. American
754 Mineralogist, 87, 245–261.
- 755 Harlov, D.E., and Förster, H.-J. (2003) Fluid-induced nucleation of (Y+REE) -phosphate
756 minerals within apatite: Nature and experiment. Part II. Fluorapatite. American Mineralogist, 88,
757 1209–1229.
- 758 Harlov, D.E., Wirth, R., and Förster, H.-J. (2005) An experimental study of dissolution–
759 reprecipitation in fluorapatite: fluid infiltration and the formation of monazite. Contributions to
760 Mineralogy and Petrology, 150, 268–286.
- 761 Harrison, T.M., and Watson, E.B. (1984) The behavior of apatite during crustal anatexis:
762 Equilibrium and kinetic considerations. *Geochimica et Cosmochimica Acta* 48, 1467-1477.
- 763 Holloway, J.R. (1971). Internally heated pressure vessels. In G.C. Ulmer, Ed. Research
764 techniques for high temperature and pressure. Springer Verlag, New York, p. 217-258.
- 765 Hoshino, M., Kimata, M., Shimizu, M., and Nishida, N. (2007) Minor-element systematics of
766 fluorapatite and zircon inclusions in allanite-(Ce) of felsic volcanic rocks from three orogenic
767 belts; implications for the origin of their host magmas. *The Canadian Mineralogist* 45, 1337-
768 1353.
- 769 Jähkel, A. (2010) Apatite contamination in the South Mountain Batholith, Nova Scotia. Unpub.
770 BSc thesis, Institute of Earth and Environmental Sciences, University of Potsdam, 60 pp.
- 771 Jung, S., Hoernes, S., and Mezger, K. (2000) Geochronology and petrogenesis of Pan-African,
772 syn-tectonic, S-type and post-tectonic A-type granite (Namibia); products of melting of crustal
773 sources, fractional crystallization and wall rock entrainment. *Lithos* 50, 259-287.
- 774 Keppler, H. (1994) Partitioning of phosphorus between melt and fluid in the system
775 haplogranite-H₂O-P₂O₅. *Chemical Geology* 117, 345-353.

- 776 Kusebauch, C., John, T., Whitehouse, M.J., Klemme, S., and Putnis, A. (2015) Distribution of
777 halogens between fluid and apatite during fluid-mediated replacement processes. *Geochimica et*
778 *Cosmochimica Acta* 170 225–246.
- 779 Lackey, J.S., Erdmann, S., Hark, J.S., Nowak, R.M., Murray, K.E., Clarke, D.B., and Valley,
780 J.W. (2011) Tracing garnet origins in granitoid rocks by oxygen isotope analysis: examples from
781 the South Mountain Batholith, Nova Scotia. *Canadian Mineralogist* 49, 417-439.
- 782 Li, H., and Hermann, J. (2017) Chlorine and fluorine partitioning between apatite and sediment
783 melt at 2.5 GPa, 800 °C: A new experimentally derived thermodynamic model. *American*
784 *Mineralogist* 102, 580–594. doi.org/10.2138/am-2017-5891.
- 785 Li, W., Chakraborty, S., Nagashima, K., and Costa, F. (2020) Multicomponent diffusion of F, Cl
786 and OH in apatite with application to magma ascent rates. *Earth Planet. Sci. Lett.* 550, 116545.
- 787 Li, W., and Costa, F. (2020) A thermodynamic model for F-Cl-OH partitioning between silicate
788 melts and apatite including non-ideal mixing with application to constraining melt volatile
789 budgets. *Geochimica et Cosmochimica Acta* 269, 203-222. doi.org/10.1016/j.gca.2019.10.035
- 790 London, D., Morgan, G.B., and Acosta-Vigil, A. (2012) Experimental simulations of anatexis
791 and assimilation involving metapelite and granitic melt. *Lithos* 153, 209-307.
- 792 London, D., Morgan, G.B. VI, Babb, H.A., and Loomis, J.L. (1993) Behavior and effects of
793 phosphorus in the system Na₂O-K₂O-Al₂O₃-SiO₂-P₂O₅-H₂O at 200 MPa (H₂O). *Contributions to*
794 *Mineralogy and Petrology* 113, 450-465.
- 795 Lux, D.R., Yates, M.G., and Gibson, D. (2006) Anonymous Interpreting magmatic conditions
796 using apatite textures and composition. *Abstracts with Programs - Geological Society of*
797 *America* Vol. 38, Iss. 7, 113.
- 798 MacDonald, M.A. (2001) *Geology of the South Mountain Batholith, Southwestern Nova Scotia.*
799 *Nova Scotia Department of Natural Resources, Mineral Resources Branch, Open File Report ME*
800 *2001-2, 262 pp.*
- 801 MacDonald, M.A., and Clarke, D.B. (2017) Occurrence, origin, and significance of melagranites
802 in the South Mountain Batholith, Nova Scotia. *Canadian Journal of Earth Sciences* 54, 693-713.

- 803 McCubbin, F.M., Vander Kaaden, K.E., Tartèse, R., Boyce, J.W., Mikhail, S., Whitson, E.S.,
804 Bell, A.S., Anand, M., Franchi, I.A., Wang, J., and Hauri, E. H (2015) Experimental
805 investigation of F, Cl, and OH partitioning between apatite and Fe-rich basaltic melt at 1.0–1.2
806 GPa and 950–1000 °C. *American Mineralogist* 100, 1790-1802. doi.org/10.2138/am-2015-5233
- 807 Morgan, G.B., and London, D., (2005) Effect of current density on the electron microprobe
808 analysis of alkali aluminosilicate glasses. *American Mineralogist* 90, 1131–1138.
809
- 810 Pan Y., and Fleet M.E. (2002) Composition of the apatite-group minerals: Substitution
811 mechanisms and controlling factors. In M. J. Kohn, J. Rakovan, and J. M. Hughes., *Phosphates:*
812 *Geochemical, Geobiological and Materials Importance*, 48, 13–49. *Reviews in Mineralogy and*
813 *Geochemistry*, Mineralogical Society of America, Washington, D.C.
814
- 815 Paton, C., Hellstrom, J, Paul, B, Woodhead, J, and Hergt, J. (2011) Iolite: Freeware for the
816 visualization and processing of mass spectrometric data. *Journal of Analytical Atomic*
817 *Spectrometry* doi:10.1039/c1ja10172b.
- 818 Piccoli, P. and Candela, P. (1992) Apatite in felsic rocks: A model for the estimation of initial
819 halogen concentrations in the Bishop Tuff (Long Valley) and Tuolumne Intrusive Suite (Sierra
820 Nevada Batholith) magmas. *American Journal of Science* 294, 92-135.
- 821 Pichavant, M., Montel, J.-M., and Richard, L.R (1992) Apatite solubility in peraluminous
822 liquids: Experimental data and an extension of the Harrison-Watson model. *Geochimica et*
823 *Cosmochimica Acta* 56, 3855-3861.
- 824 Rizkalla, A.S., Jones, D.W., Hall, G.C., and Sutow, E.J. (1991) Composition of feldspathic glass
825 synthesized by sol-gel. *British Ceramic Transactions and Journal*, 90, 81-84.
- 826 Schettler, G., Gottschalk, M., and Harlov, D.E. (2011) A new semi-micro wet chemical method
827 for apatite analysis and its application to the crystal chemistry of fluorapatite-chlorapatite solid
828 solutions. *American Mineralogist* 96, 138–152.
- 829 Stock, M.J., Humphreys, M.C.S., Smith, V.C., Johnson, R.D., Pyle, D.M., and EIMF. (2015)
830 New constraints on electron-beam induced halogen migration in apatite. *American Mineralogist*
831 100, 281-293

- 832 Stokes, T.N., Bromileya, G.D., Potts, N.J., Saunders, K.E., and Miles, A.J. (2019) The effect of
833 melt composition and oxygen fugacity on manganese partitioning between apatite and silicate
834 melt. *Chemical Geology* 506, 162-174.
- 835 Stormer, J.C., Pierson, M.L., and Tacker, R.C. (1993) Variation of F and Cl X-ray intensity due
836 to anisotropic diffusion in apatite during electron microprobe analysis. *American Mineralogist*
837 78, 641-648.
- 838 Sun, J-F., Yang, J-H., Zhang, J-H., Yang, Y-H., and Zhu, Y-S. (2021) Apatite geochemical and
839 Sr Nd isotopic insights into granitoid petrogenesis. *Chemical Geology* 566, 120104.
- 840 Tollari, N., Toplis, M.J., and Barnes, S.-J. (2006) Predicting phosphate saturation in silicate
841 magmas: An experimental study of the effects of melt composition and temperature. *Geochimica*
842 *et Cosmochimica Acta* 70, 1518-1536.
- 843 Watson, E.B., and Green, T.H. (1981) Apatite/liquid partition coefficients for the rare earth
844 elements and strontium. *Earth and Planetary Science Letters*. 56, 405-421.
- 845 Webster, J.D. (1992) Water solubility and chlorine partitioning in Cl-rich granitic systems:
846 Effects of melt composition at 2 kbar and 800°C. *Geochimica et Cosmochimica Acta* 56, 679-
847 687.
- 848 Webster, J.D., Goldoff, B.A., Flesch, R.N., Nadeau, P.A., and Silbert, Z.W. (2017) Hydroxyl, Cl,
849 F partitioning between high-silica rhyolitic melts-apatite-fluid(s) at 50-200 MPa and 700-
850 1000°C. *American Mineralogist* 102, 61-74.
- 851 Webster, J.D., and Piccoli, P.M. (2015) Magmatic apatite; a powerful, yet deceptive, mineral.
852 *Elements* 11, 177-182.
- 853 Webster, J.D., Tappen, D., and Mandeville, C.W. (2009) Partitioning behavior of chlorine and
854 fluorine in the system apatite-melt-fluid: II. Felsic silicate systems at 200 MPa. *Geochimica et*
855 *Cosmochimica Acta* 73, 559-581.
- 856 Webster J.D., Vetere F., Botcharnikov R.E., Goldoff, B., McBirney A., and Doherty A.L. (2015)
857 Experimental and modeled chlorine solubilities in aluminosilicate melts at 1 to 7000 bars and
858 700 to 1250 C Applications to magmas of Augustine Volcano, Alaska. *American Mineralogist*
859 100, 522–535.
- 860 Wolf, M.B., and London D. (1994) Apatite dissolution into peraluminous haplogranitic melts:
861 An experimental study of solubilities and mechanisms. *Geochimica et Cosmochimica Acta* 58,
862 4127-4145.

- 863 Wolf, M.B., and London, D. (1995) Incongruent dissolution of REE- and Sr-rich apatite in
864 peraluminous granitic liquids: Differential apatite, monazite, and xenotime solubilities during
865 anatexis. *American Mineralogist* 80, 765-775.
- 866 Wones, D.R. (1989) Significance of the assemblage titanite+magnetite+quartz in granitic rocks.
867 *American Mineralogist* 74, 744-749.
- 868 Wudarska, A., Słaby, E., Wiedenbeck, M., Barnes, J.D., Bonifacie, M., Sturchio, N.C., and
869 others (2021). Inter-laboratory Characterisation of Apatite Reference Materials for Chlorine
870 Isotope Analysis. *Geostandards and Geoanalytical Research*, 45(1), 121-142.
- 871 Xu, B., Kou, G., Etschmann, B., Liu, D., and Brugger, J. (2020) Spectroscopic, Raman, EMPA,
872 Micro-XRF and Micro-XANES Analyses of Sulphur Concentration and Oxidation State of
873 Natural Apatite Crystals. *Crystals* 10, 1032. <https://doi.org/10.3390/cryst10111032>.

874 **Figure Captions**

875 **Figure 1:** Preliminary experiments at 750 °C, 200 MPa, and 2000 h. (a) large grain of Durango
876 apatite showing Cl diffusion gradient over a distance of 20 μm toward its margin. The apatite
877 grain boundary with the silicate melt is not detectable on the Cl line scan. The apatite appears to
878 be losing Cl to the silicate melt and is presumably gaining OH because the F profile appears
879 unchanged. (b) Even this small apparently detached satellite apatite grain is not homogenized
880 with respect to Cl. White lines in both images highlight the microprobe line scan.

881

882 **Figure 2:** Plot of apatite run products as a function of F and Cl for experimental runs with two
883 starting apatite compositions. Apatite compositions in ‘wet’ runs have lower Cl and higher OH
884 concentrations than those in the corresponding ‘dry’ runs. Stoichiometric Cl-Ap has 0.192 mol
885 Cl, stoichiometric F-Ap has 0.198 mol F, and stoichiometric OH-Ap has 0.195 mol OH. For
886 representational simplicity, all these mol fractions are rounded to 0.200 in [Figures 2](#) and [4](#).

887

888 **Figure 3:** REE concentrations in 30 run-product apatite grains from each experiment containing
889 two starting apatite compositions, including the Durango apatite. The wide range of ΣREE in the
890 Durango apatite is a measure of its inhomogeneity; the wider range of ΣREE in the experimental
891 run apatites is a measure of the failure of the system to attain chemical equilibrium with respect
892 to the REE.

893

894 **Figure 4:** Plot of apatite run products as a function of F and Cl for experimental runs containing
895 three starting apatite compositions. Apatite compositions in the ‘wet’ runs have lower Cl
896 concentrations than those in the corresponding ‘dry’ runs. The effect of added H₂O is to increase
897 the concentration of OH in the apatite and to lower the Cl/F ratio in the apatite run products,
898 suggesting that Cl is preferentially partitioned into a separate fluid phase.

899

900 **Figure 5:** REE concentrations in 30 run-product apatite grains for all experiments containing
901 three starting apatite compositions. The wide range of Σ REE in the Durango apatite is a measure
902 of its inhomogeneity; the wider range of Σ REE in the experimental run apatites is a measure of
903 the failure of the system to attain chemical equilibrium with respect to the REE. The greater
904 scatter in Cl concentrations for apatites from the ‘dry’ runs than from the ‘wet’ runs suggests that
905 a separate fluid phase may be responsible for increasing the rate of anion exchange.

906

907 **Figure 6:** Images of experimental glasses. (a) ‘Dry’ run AA-9 with some small bubbles.
908 (b) ‘Wet’ run AA-12 with abundant large bubbles. The only solid phase is apatite.

909

910 **Figure 7.** Diffusion Profiles. (a) Calculated concentration as a function of distance for the
911 diffusive uptake of Cl into a spherical grain of apatite with a radius of 50 μ m. Model curves are
912 calculated for a temperature of 1200 °C using the diffusion parameters (D_o , E_a) measured by
913 Brenan (1994) assuming an initial Cl concentration of 0.43 wt% and an equilibrium
914 concentration of 2.2 wt%. The initial value corresponds to the average Durango apatite starting
915 material, and the equilibrium concentration is assumed to be the final concentration of apatite in

916 experiment AA-14. Curves are labelled according to the time in hours. (b) Calculated
917 concentration as a function of distance for the diffusive uptake of REE (sum of $\text{La}_2\text{O}_3 + \text{Ce}_2\text{O}_3$)
918 into a spherical grain of apatite with a radius of 50 μm (note the change of x-axis scale compared
919 to Figure 7a (above). Model curves are calculated for a temperature of 1200 °C using the
920 diffusion parameters (D_o , E_a) reported by Cherniak (2000) assuming an initial $\text{La}_2\text{O}_3 + \text{Ce}_2\text{O}_3$
921 concentration of 0.998 wt% and an equilibrium concentration of 0.2 wt%. The initial value
922 corresponds to the average Durango apatite starting material and the equilibrium value at the
923 crystal margin is calculated assuming a $D^{\text{apatite/melt}}$ of 15 and a melt $\text{La}_2\text{O}_3 + \text{Ce}_2\text{O}_3$ concentration
924 of 0.013 wt%. Curves are labeled according to the time in hours.

925

926 **Figure 8:** BSE images of experimental run products from experiments AA-9 through AA-14
927 involving two starting apatite compositions. Apatite grains in each of the six runs show
928 significant rounding of their original shard shapes, presumably caused by chemical dissolution.
929 Some of the apatite grains show the development of crystal faces (white arrows), probably as
930 epitaxial overgrowths on the original anhedral grains, which serves as evidence of their approach
931 to textural equilibrium. In addition, many grains show slightly lighter-colored rims that may
932 indicate diffusion-controlled compositional differences prior to reaching either chemical or
933 textural equilibrium.

934

935 **Figure 9:** BSE images of run products from experiments AA-15 through AA-18 involving three
936 starting apatite compositions. Runs AA-15 and AA-16 are ‘dry’ and ‘wet’, respectively, and all
937 starting materials were finely ground. Runs AA-17 and AA-18 are ‘dry’ and ‘wet’, respectively,

938 and the SANK 1.3 gel was the only finely ground starting material. Run AA-18 contains rare
939 euhedral grains (white arrow), and some clusters of either skeletal/quench apatite grains or
940 apatite grains that have undergone differential dissolution, outlining a rough apatite shape (white
941 arrows with question marks).

942

943 **Figure 10:** Schematic representation of the physical and chemical approaches to equilibrium. In
944 the experiments, and in nature, the processes behind the attainment of chemical equilibrium
945 involve dissolution into the silicate melt, diffusion through the silicate melt, followed by
946 chemical exchange and solid-state diffusion in the apatite grains. Physical/textural equilibrium is
947 attained by changes in shape from shards to round to euhedral, from many to few by Ostwald
948 ripening, and from anhedral to euhedral by epitaxial overgrowth.

949

950 **Figure 11:** Naturally occurring apatite grains in granite sample P7G3 representing a microcosm
951 of the contamination process. (a-c) Chain of apatite grains extending in both directions from
952 within a small xenolith (dashed outline) into the enclosing granite. Apatite grains in the xenolith
953 are small and anhedral. Apatite grains in the granite are large and more euhedral. (d) Four large,
954 subhedral to euhedral, and texturally apparently magmatic, apatite grains in granite sample P7G3
955 outside the chain. (e) CCL image of country-rock sample P6C1 showing a band of ultra-fine-
956 grained apatite. PPL – plane polarized light; BSE – backscattered electrons; CCL – color
957 cathodoluminescence.

958

959 **Figure 12:** Apatite grain compositions in granite sample P7G3, showing cores and rims (joined
960 by arrows) with respect to Ce_2O_3 vs. Y_2O_3 (a), and FeO vs. MnO (b). The dashed green ellipses
961 contain the cores of the smallest and most anhedral metamorphic apatite grains (A-4 to A-7) in
962 the xenolith (as in Figures 11a,b,c). Boxes summarize core-rim vector quadrants: UL – up left;
963 UR – up right; DL – down left; DR – down right.

Table 1. Experimental conditions

Run	T (°C)	P (MPa)	t (hours)	SANK1.3 (mg)	F-Ap (mg) ^a	Cl-Ap (mg) ^b
AA-9	1200	2	192	21.82	1.09	1.09
AA-10	1200	2	192	21.82	1.09	
AA-11	1200	2	192	21.82		1.09
AA-12	1200	2	192	20.94	1.05	1.05
AA-13	1200	2	192	20.94	1.05	
AA-14	1200	2	192	20.94		1.05
AA-15	1200	2	192	21.82	0.73	0.73
AA-16	1200	2	192	20.91	0.71	0.71
AA-17	1200	2	192	18.50	0.53	0.62
AA-18	1200	2	192	17.46	0.54	0.59

a - synthetic fluorapatite APS-64; b - synthetic chlorapatite APS-65; c - Durango fluorapatite
 * - ratio of amount of apatite relative to starting granitic gel by mass.

D-Ap (mg) ^c	Added H ₂ O (mg)	Ap/Gel*
	0.00	0.10
1.09	0.00	0.10
1.09	0.00	0.10
	0.96	0.10
1.05	0.96	0.10
1.05	0.96	0.10
0.73	0.00	0.10
0.71	0.96	0.10
0.57	0.00	0.10
0.5	0.80	0.10

e.

Table 2. Operating conditions for electron microprobe analysis of apatite

Element	Calibration Material	Source	Spectral Line/Diffracting Crystal
Ca, P	Apatite, natural	Durango	K α /PETJ
F	Fluorite, natural	Astimex	K α /LDE1
Cl	Tugtupite, natural		K α /PETH
La	LaPO ₄ , synthetic	Smithsonian	L α /LIF
Ce	CePO ₄ , synthetic		

Counting Time (s)
Peak/Background

10/10

10/10

40/60

Table 3. Operating conditions for electron microprobe analysis of peraluminous granite g

Element	Calibration Material	Source	Spectral Line/Diffracting Crystal
Ca, P	Apatite, natural	Durango	K α / PETL/ PETH
Cl	Tugtupite, natural		K α / PETH
Mn	Rhodonite, natural		K α / LIFL
Si	Quartz, natural	Astimex	K α / TAP
Na	Albite, natural		K α / TAPL
F	Fluorite, natural		K α / LDE1L
Al, K	Orthoclase, natural	GeoMK	K α / TAP/ PETL
Fe	Hematite, natural		K α / LIFL
Ce	CePO ₄ , artificial	Smithsonian	L α / LIF
La	LaPO ₄ , artificial		

lasses

Counting Time (s)
Peak/Background

20 / 20, 30 / 30
20 / 20

10/10

30 / 30

Table 4. Mean compositions of run-product apatite grains in experiments with two starting apatite compo

Run	Start	n	F (wt%)	1 σ	Cl (wt%)	1 σ	F (mol)	Cl (mol)
AA-9	F-Ap + Cl-Ap	36	2.49	0.15	1.34	0.04	0.131	0.038
AA-10	F-Ap + D-Ap	30	3.33	0.13	0.09	0.01	0.175	0.003
AA-11	Cl-Ap+ D-Ap	31	1.08	0.13	3.23	0.06	0.057	0.091
AA-12	F-Ap + Cl-Ap	32	2.70	0.22	0.59	0.05	0.142	0.017
AA-13	F-Ap + D-Ap	31	3.09	0.14	0.05	0.01	0.162	0.001
AA-14	Cl-Ap+ D-Ap	32	0.84	0.11	2.17	0.07	0.044	0.061
Stoich F-Ap	*	*	3.77	*	0.00	*	0.198	0.000
Stoich Cl-Ap	*	*	0.00	*	6.81	*	0.000	0.192
D-Ap	*	13	3.39	0.15	0.43	0.04	0.178	0.012
Initial 9-12	F-Ap + Cl-Ap	*	1.89	*	3.41	*	0.099	0.096
Initial 10-13	F-Ap + D-Ap	*	3.58	*	0.22	*	0.188	0.006
Initial 11-14	Cl-Ap+ D-Ap	*	1.70	*	3.62	*	0.089	0.102

Apatite analyses are of randomly oriented grains in the experimental run. Part of the spread in F concentration is due to grain orientation (Stormer et al. 1993). The most reliable halogen parameter is Cl. F-Ap – synthetic F-apatite; Cl-Ap – synthetic Cl-apatite; D-Ap – synthetic D-apatite.

ositions

OH Diff (mol)	F (mol %)	Cl (mol %)	OH (mol %)
0.026	67.24	19.40	13.36
0.017	89.77	1.35	8.87
0.047	29.16	46.77	24.07
0.036	72.77	8.58	18.65
0.031	83.29	0.71	16.00
0.089	22.77	31.37	45.86
-0.003	101.77	0.00	-1.77
0.003	0.00	98.51	1.49
0.004	91.51	6.22	2.27
0.000	50.88	49.25	-0.14
0.000	96.64	3.11	0.25
0.004	45.75	52.36	1.88

rations is EMPA analytical error, and another part is apatite
Cl-Ap – synthetic Cl-apatite; D-Ap – natural Durango apatite

Table 5. Average compositions of initial and run-product apatite grains in experiments with three start

Run	n	F (wt%)	1 σ	Cl (wt%)	1 σ	F (mol)	Cl (mol)	OH Diff (mol)
AA-15	31	2.72	0.16	1.20	0.06	0.143	0.034	0.018
AA-16	31	2.16	0.12	0.96	0.04	0.114	0.027	0.054
AA-17	31	2.53	0.17	1.37	0.14	0.133	0.039	0.023
AA-18	34	2.54	0.13	0.72	0.03	0.134	0.020	0.041
F-Ap	11	3.77	0.29	0.00	0.01	0.198	0.000	-0.003
Cl-Ap	9	0.00	0.00	6.81	0.11	0.000	0.192	0.003
D-Ap	13	3.39	0.15	0.43	0.04	0.178	0.012	0.004
Initial Bulk		2.39		2.41		0.13	0.07	0.00

ting apatite compositions

F (mol %)	Cl (mol %)	OH (mol %)
73.42	17.40	9.18
58.43	13.87	27.70
68.29	19.77	11.93
68.46	10.46	21.08
101.77	0.00	-1.77
0.00	98.51	1.49
91.51	6.22	2.27
64.42	34.91	0.67

Table 6. Mean major-element compositions of glasses from runs AA-9 'dry' and AA-12 'wet'

	SANK 1.3* (wt%)	AA-9** (wt%)	1 σ	AA-12** (wt%)	1 σ
n		10		10	
SiO ₂	77.56	74.25	0.95	74.25	1.33
Al ₂ O ₃	14.25	14.49	0.11	14.47	0.19
CaO	0.00	1.83	0.04	1.93	0.01
Na ₂ O	3.72	4.00	0.11	3.89	
K ₂ O	4.47	4.47	0.04	4.65	0.04
P ₂ O ₅ meas	0.00	0.74	0.03	0.57	0.02
P ₂ O ₅ adj***		1.37		1.44	
F	0.00	0.00		0.00	
Cl	0.00	0.23	0.01	0.23	0.01
Total	100.00	101.38		101.43	
A/CNK****	1.30	0.98		0.97	

*Nominal.

**Normalized to anhydrous.

*** P₂O₅ adj = CaO/1.34. Explanation in text.

**** A/CNK = mol (Al₂O₃/(CaO+Na₂O+K₂O)).

Table 7. Rare earth element concentration in run-product glasses and Durango apatite (mg/g)

Experiment	n	La	Ce	Pr	Nd	Sm	Eu	Gd	Tb	Dy	Ho	Er	Tm	Yb	Lu
AA-10	4	48.03	66.18	3.69	9.63	1.18	0.19	1.18	0.12	0.80	0.19	0.44	0.067	0.48	0.059
1 σ		8.32	6.33	0.75	2.36	0.37	0.04	0.29	0.05	0.23	0.06	0.22	0.015	0.12	0.009
AA-13	3	48.61	67.06	4.03	10.76	1.51	0.15	1.32	0.13	0.83	0.21	0.63	0.08	0.58	0.05
1 σ		2.11	3.94	0.12	0.77	0.49	0.03	0.06	0.02	0.13	0.07	0.14	0.00	0.10	0.00
Durango	7	3658.45	4772.30	346.93	1107.07	158.08	15.92	151.99	18.05	105.35	20.82	57.75	7.02	38.75	4.75
1 σ		184.16	269.08	14.62	55.23	8.21	1.26	9.54	1.26	7.21	1.22	4.15	0.54	2.60	0.26

Table 8. Model parameters

Species	Do (m ² /s)	Ea (kJ/mol)	apatite/melt partition coefficient	D 1200°C (m ² /s)	references
REE	2.60E-07	-324	15	8.44E-19	a,b
Cl-F-OH	1.60E-04	-284	---	1.36E-14	c
Cl	7.00E-05	-294	---	2.63E-15	d

Notes:

a: Values are for La diffusion reported by Cherniak (2000).

b: Partition coefficient for Sm estimated from the variation in apatite/melt partitioning with melt SiO₂ concentration from Watson and Green (1981).

c: Values parallel to c-axis from Brenan (1994).

d: Values for Cl self diffusion reported by Li et al (2020).

Table 9. Compositions (wt %) for cores and rims of the apatite grains from granite sample P7G3

Apatite	Core/Rim	SO ₃	P ₂ O ₅	SiO ₂	Y ₂ O ₃	La ₂ O ₃	Ce ₂ O ₃	Pr ₂ O ₃
A1	Core	0.01	42.26	0.12	0.35	0.02	0.26	0.00
A2	Core	0.00	42.58	0.01	0.17	0.01	0.06	0.06
A3	Core	0.31	39.89	0.10	0.30	0.02	0.09	0.00
A4	Core	0.01	42.06	0.16	0.28	0.07	0.15	0.00
A5	Core	0.00	41.97	0.10	0.30	0.00	0.15	0.01
A6	Core	0.00	42.18	0.09	0.34	0.02	0.14	0.08
A7	Core	0.00	42.12	0.14	0.33	0.00	0.15	0.06
A8	Core	0.00	41.98	0.15	0.39	0.07	0.17	0.13
A9	Core	0.01	42.65	0.15	0.34	0.00	0.15	0.00
A10	Core	0.01	42.08	0.10	0.36	0.06	0.07	0.02
A12	Core	0.00	42.04	0.14	0.32	0.06	0.11	0.00
A11R	Core	0.13	41.65	0.28	0.29	0.05	0.13	0.02
G1	Core	0.00	42.53	0.02	0.08	0.02	0.04	0.00
C1	Core	0.00	42.05	0.07	0.34	0.01	0.13	0.01
C2	Core	0.00	41.90	0.14	0.27	0.02	0.10	0.09
D1	Core	0.00	42.82	0.10	0.32	0.02	0.11	0.00
Mean	Core	0.03	42.05	0.12	0.30	0.03	0.13	0.03
1σ		0.08	0.65	0.06	0.08	0.03	0.05	0.04
A1	Rim	0.01	42.25	0.06	0.29	0.04	0.18	0.00
A2	Rim	0.00	42.47	0.04	0.09	0.00	0.08	0.00
A3	Rim	0.25	40.03	0.13	0.17	0.00	0.04	0.16
A4	Rim	0.01	42.00	0.11	0.24	0.06	0.06	0.00
A5	Rim	0.00	42.22	0.11	0.27	0.00	0.04	0.07
A6	Rim	0.00	41.99	0.10	0.33	0.06	0.13	0.00
A7	Rim	0.01	42.02	0.14	0.32	0.00	0.12	0.20
A8	Rim	0.00	42.19	0.06	0.23	0.02	0.12	0.03
A9	Rim	0.00	42.43	0.08	0.33	0.00	0.13	0.00
A10	Rim	0.01	41.93	0.15	0.29	0.09	0.13	0.02
A12	Rim	0.02	42.04	0.10	0.24	0.05	0.08	0.00
G1	Rim	0.01	42.38	0.04	0.05	0.01	0.03	0.09
C1	Rim	0.01	42.15	0.03	0.29	0.06	0.11	0.04
C2	Rim	0.00	42.06	0.13	0.30	0.00	0.13	0.02
D1	Rim	0.00	42.34	0.11	0.25	0.04	0.11	0.00
Mean	Rim	0.02	42.01	0.09	0.25	0.03	0.10	0.05

1 σ

0.07

0.60

0.04

0.09

0.03

0.04

0.07

* - estimated by charge balance on the halogen site.

Nd ₂ O ₃	MgO	CaO	MnO	FeO	Na ₂ O	F	Cl	H ₂ O*
0.19	0.10	53.59	0.92	0.63	0.22	3.36	0.14	0.33
0.01	0.06	54.48	0.84	0.45	0.11	3.40	0.12	0.32
0.14	0.04	50.66	0.70	0.53	0.53	2.84	0.11	0.67
0.11	0.04	54.50	0.82	0.42	0.18	3.40	0.11	0.31
0.07	0.04	54.44	0.82	0.46	0.26	3.46	0.08	0.26
0.12	0.05	54.04	0.93	0.42	0.20	3.40	0.13	0.30
0.06	0.06	54.44	0.84	0.43	0.19	3.56	0.10	0.16
0.18	0.06	53.72	0.94	0.67	0.16	3.42	0.15	0.26
0.18	0.05	53.87	0.97	0.38	0.22	3.26	0.09	0.48
0.07	0.03	54.28	0.86	0.43	0.21	3.32	0.09	0.39
0.08	0.05	54.34	0.76	0.55	0.15	3.51	0.10	0.20
0.04	0.04	54.20	0.71	0.81	0.16	3.63	0.06	0.10
0.00	0.01	55.86	0.28	0.05	0.05	3.92	0.02	
0.10	0.05	54.08	0.94	0.43	0.22	3.51	0.13	0.18
0.07	0.05	54.35	0.74	0.52	0.10	3.49	0.07	0.23
0.07	0.01	54.98	0.69	0.26	0.21	3.55	0.09	0.22
0.09	0.05	54.11	0.80	0.46	0.20	3.44	0.10	0.27
0.06	0.02	1.06	0.17	0.17	0.10	0.22	0.03	
0.08	0.07	53.78	0.87	0.48	0.22	3.24	0.12	0.46
0.10	0.05	54.88	0.68	0.42	0.05	3.40	0.11	0.33
0.08	0.04	51.82	0.69	0.63	0.21	3.04	0.12	0.50
0.04	0.04	54.68	0.72	0.48	0.17	3.56	0.11	0.15
0.03	0.05	54.69	0.72	0.44	0.18	3.66	0.06	0.09
0.08	0.04	54.25	0.86	0.45	0.21	3.54	0.09	0.17
0.10	0.06	54.29	0.77	0.55	0.20	3.53	0.07	0.20
0.06	0.08	54.15	0.94	0.61	0.21	3.46	0.15	0.23
0.09	0.06	54.01	0.88	0.42	0.11	3.45	0.10	0.27
0.12	0.08	54.23	0.77	0.51	0.22	3.46	0.08	0.26
0.09	0.05	54.66	0.74	0.55	0.06	3.61	0.09	0.11
0.04	0.00	55.86	0.28	0.04	0.00	3.82	0.02	
0.08	0.05	53.99	0.84	0.46	0.08	3.47	0.10	0.23
0.11	0.04	54.29	0.74	0.61	0.18	3.42	0.06	0.31
0.11	0.05	54.93	0.64	0.26	0.20	3.73	0.06	0.03
0.08	0.05	54.26	0.75	0.48	0.15	3.48	0.09	0.23

0.03

0.02

0.87

0.16

0.14

0.08

0.18

0.03

Sum	F=O	Cl=O	Total
102.49	1.41	0.03	101.04
102.69	1.43	0.03	101.23
96.62	1.20	0.02	95.40
102.63	1.43	0.02	101.17
102.43	1.46	0.02	100.95
102.43	1.43	0.03	100.97
102.64	1.50	0.02	101.12
102.44	1.44	0.03	100.97
102.80	1.37	0.02	101.41
102.37	1.40	0.02	100.95
102.42	1.48	0.02	100.92
102.17	1.53	0.01	100.62
102.88	1.65	0.01	101.23
102.24	1.48	0.03	100.73
102.14	1.47	0.02	100.66
103.44	1.49	0.02	101.92
102.17	1.45	0.02	100.70
102.13	1.36	0.03	100.74
102.71	1.43	0.02	101.25
97.68	1.28	0.03	96.37
102.43	1.50	0.03	100.91
102.64	1.54	0.01	101.09
102.28	1.49	0.02	100.77
102.58	1.49	0.02	101.07
102.54	1.46	0.03	101.05
102.36	1.45	0.02	100.88
102.33	1.46	0.02	100.86
102.47	1.52	0.02	100.93
102.65	1.61	0.00	101.04
102.00	1.46	0.02	100.51
102.40	1.44	0.01	100.95
102.87	1.57	0.01	101.29
102.08	1.46	0.02	100.60

Table 10. Average halogen concentrations (wt %) in all apatite grains in granite P7G3, regardless of apparent origin (magmatic or xenocrystic)

	n	Core	1 σ	Rim	1 σ
F	16	3.44	0.22	3.53	0.22
Cl	15	0.10	0.03	0.09	0.03

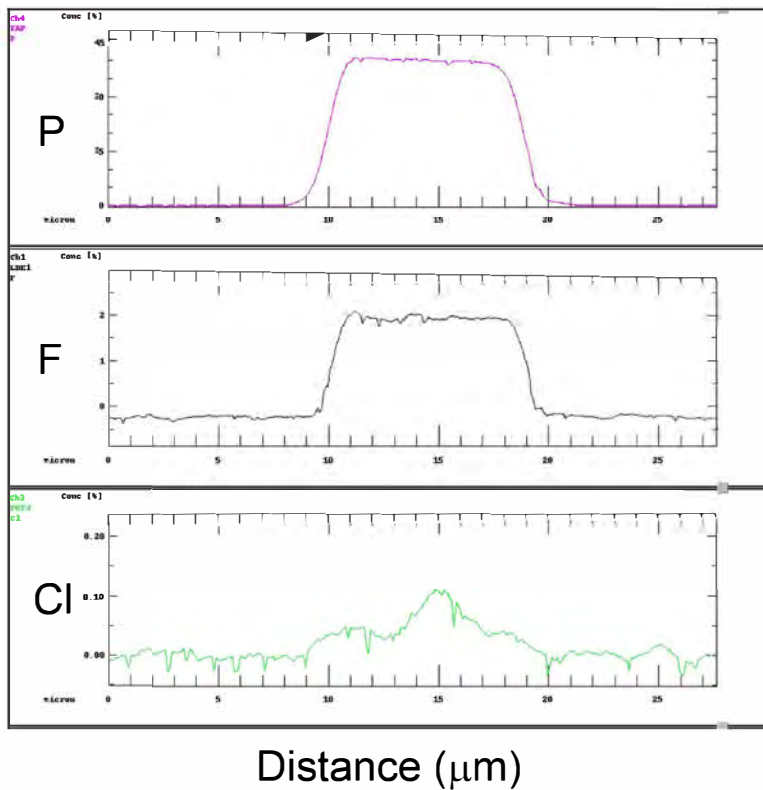
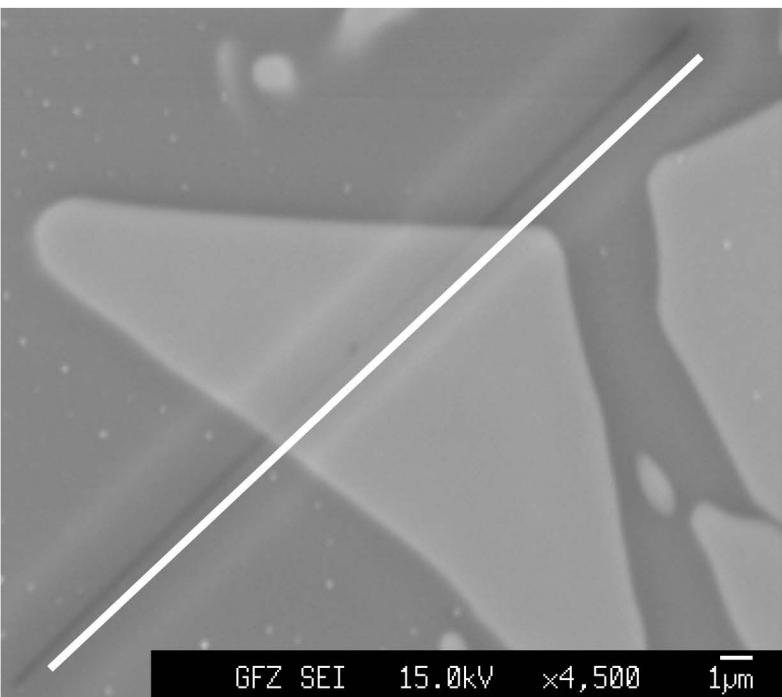
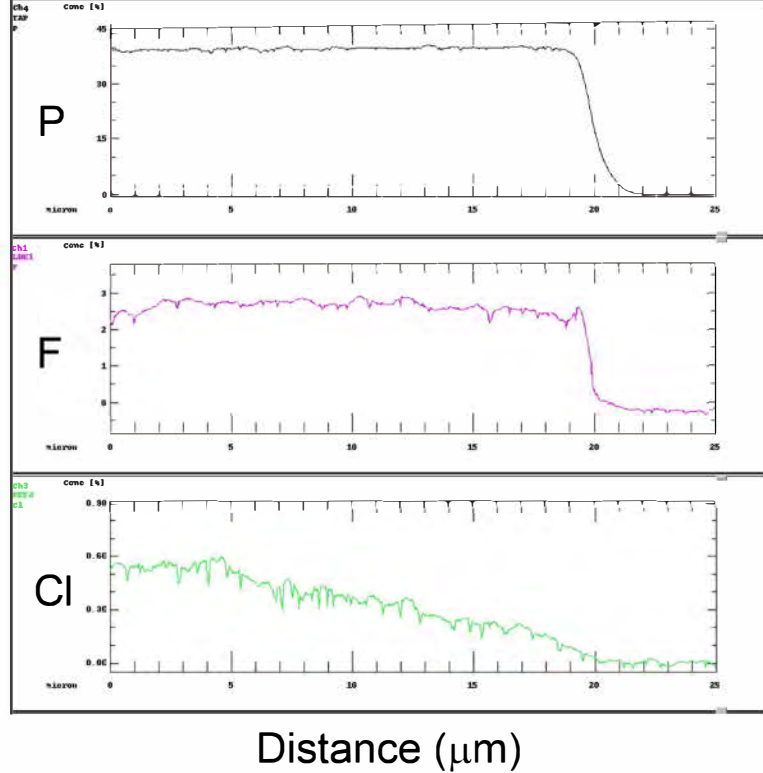
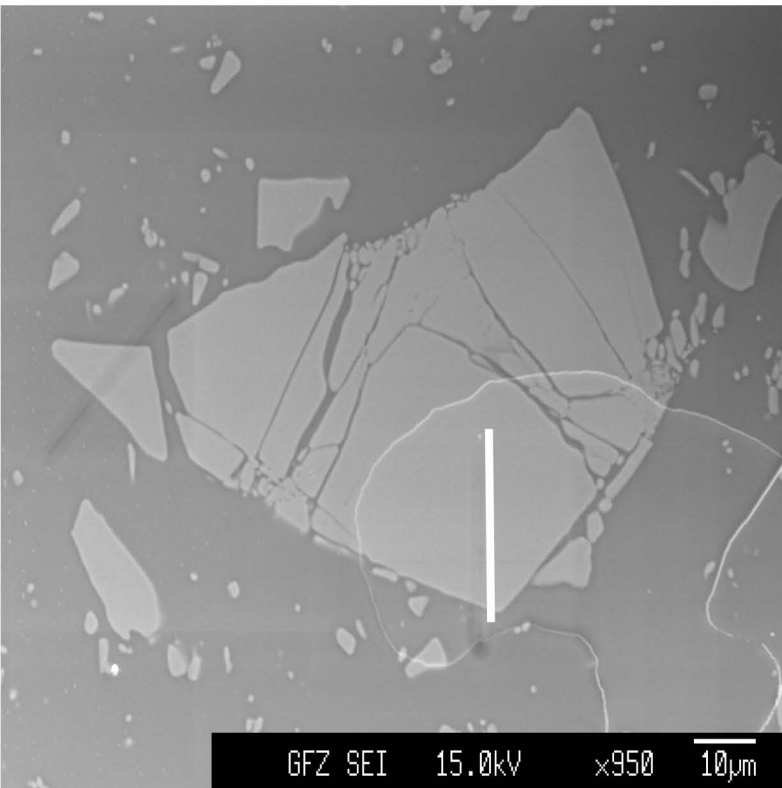


Figure 1

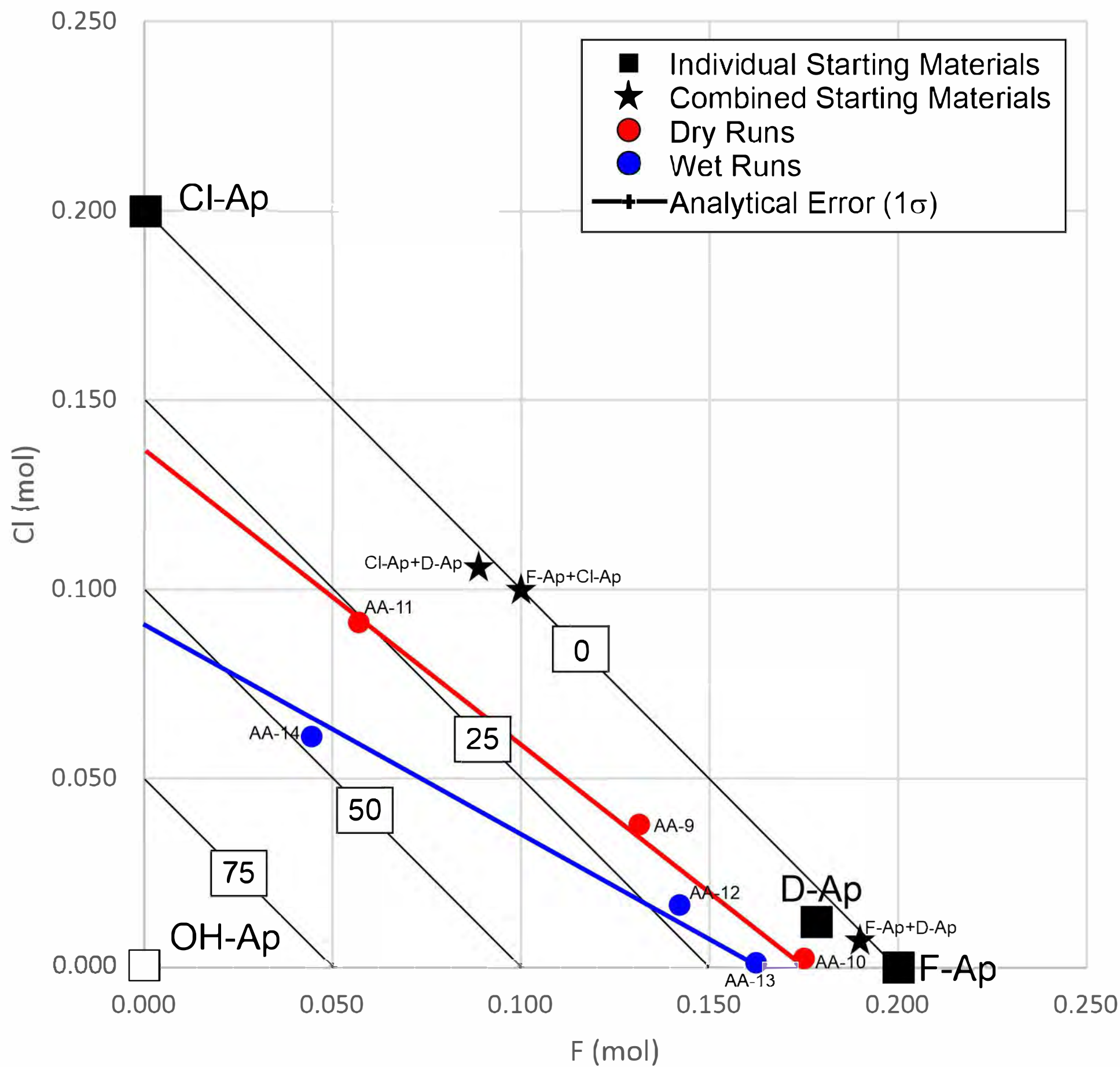


Figure 2

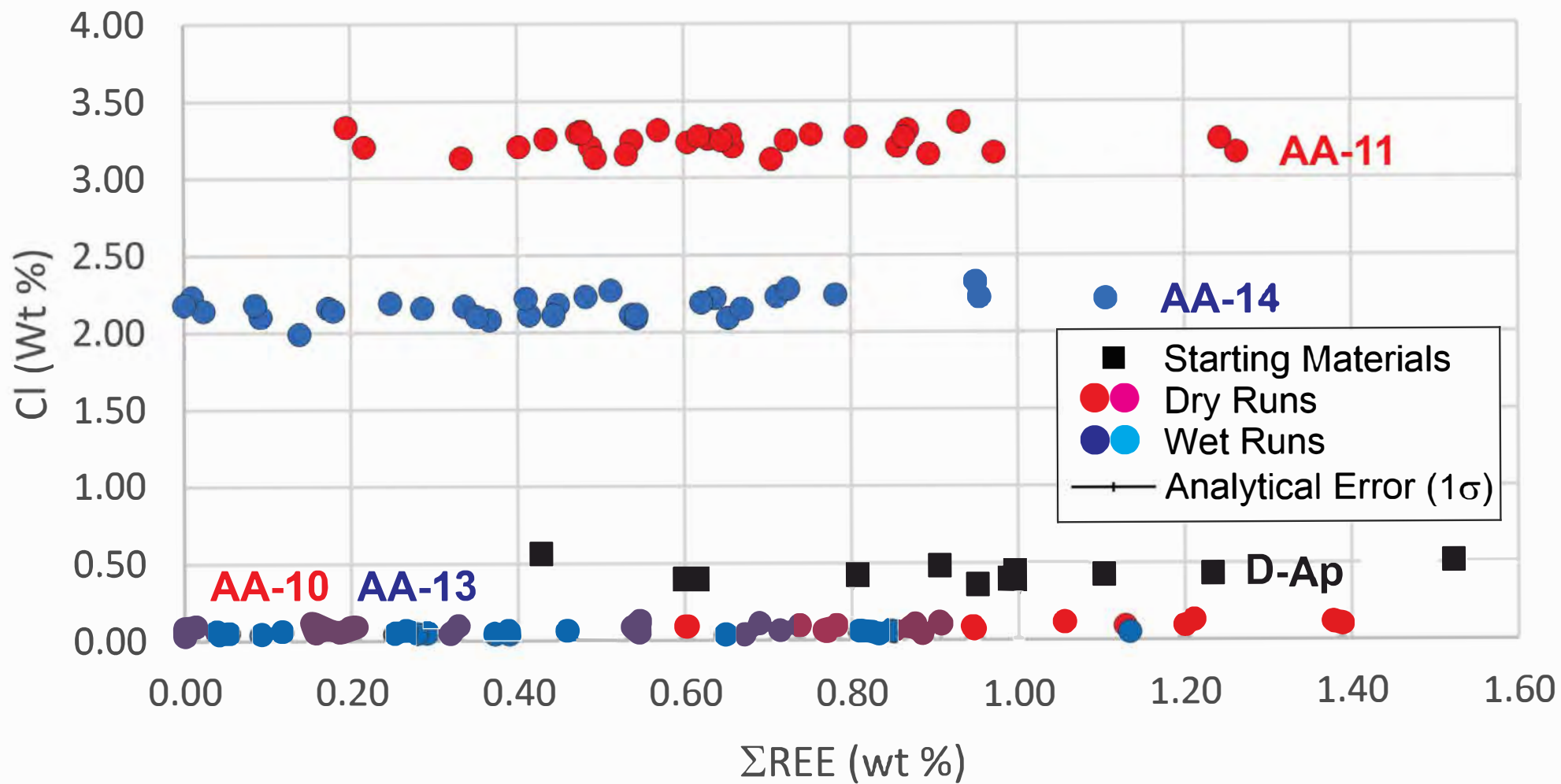


Figure 3

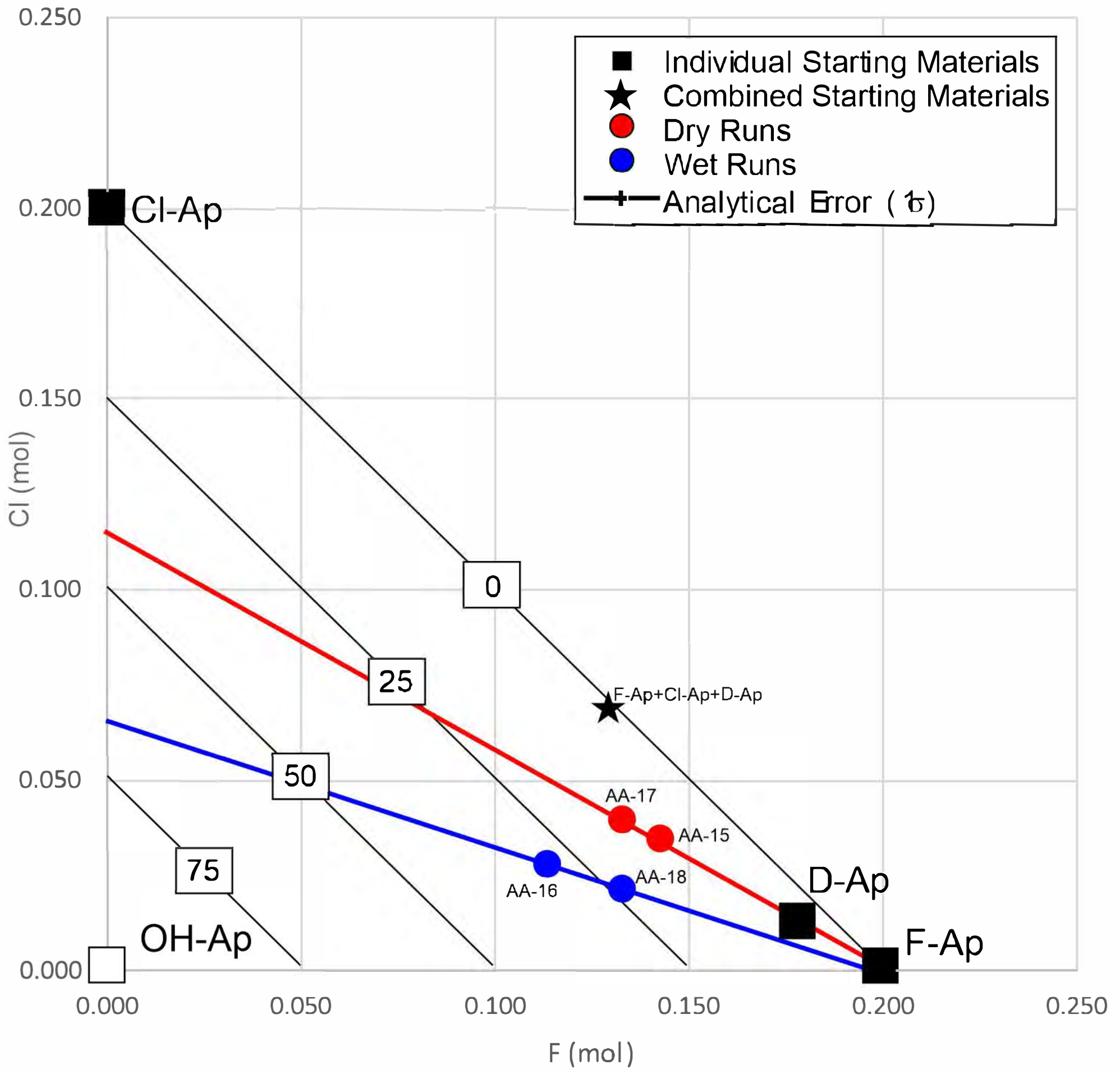


Figure 4

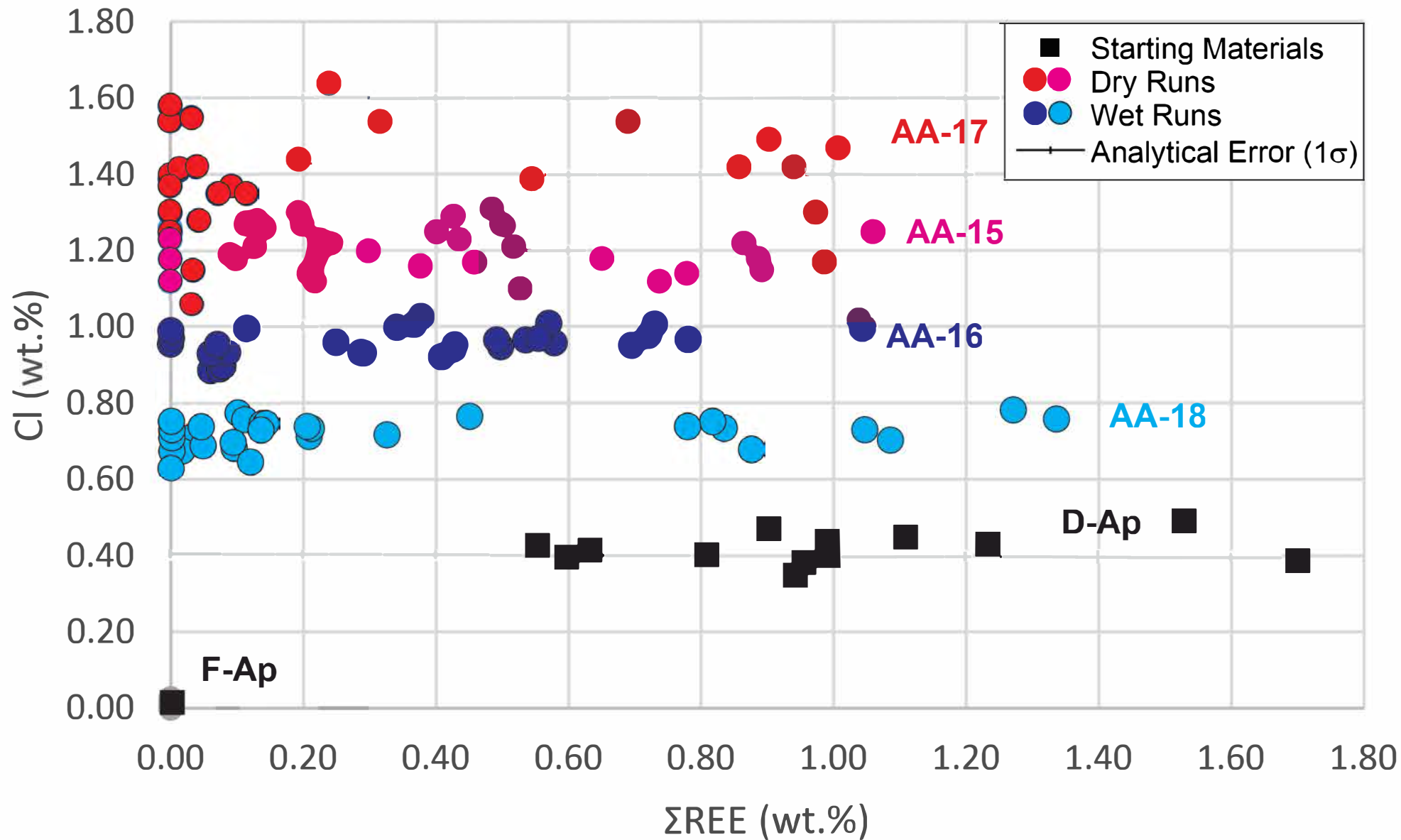


Figure 5

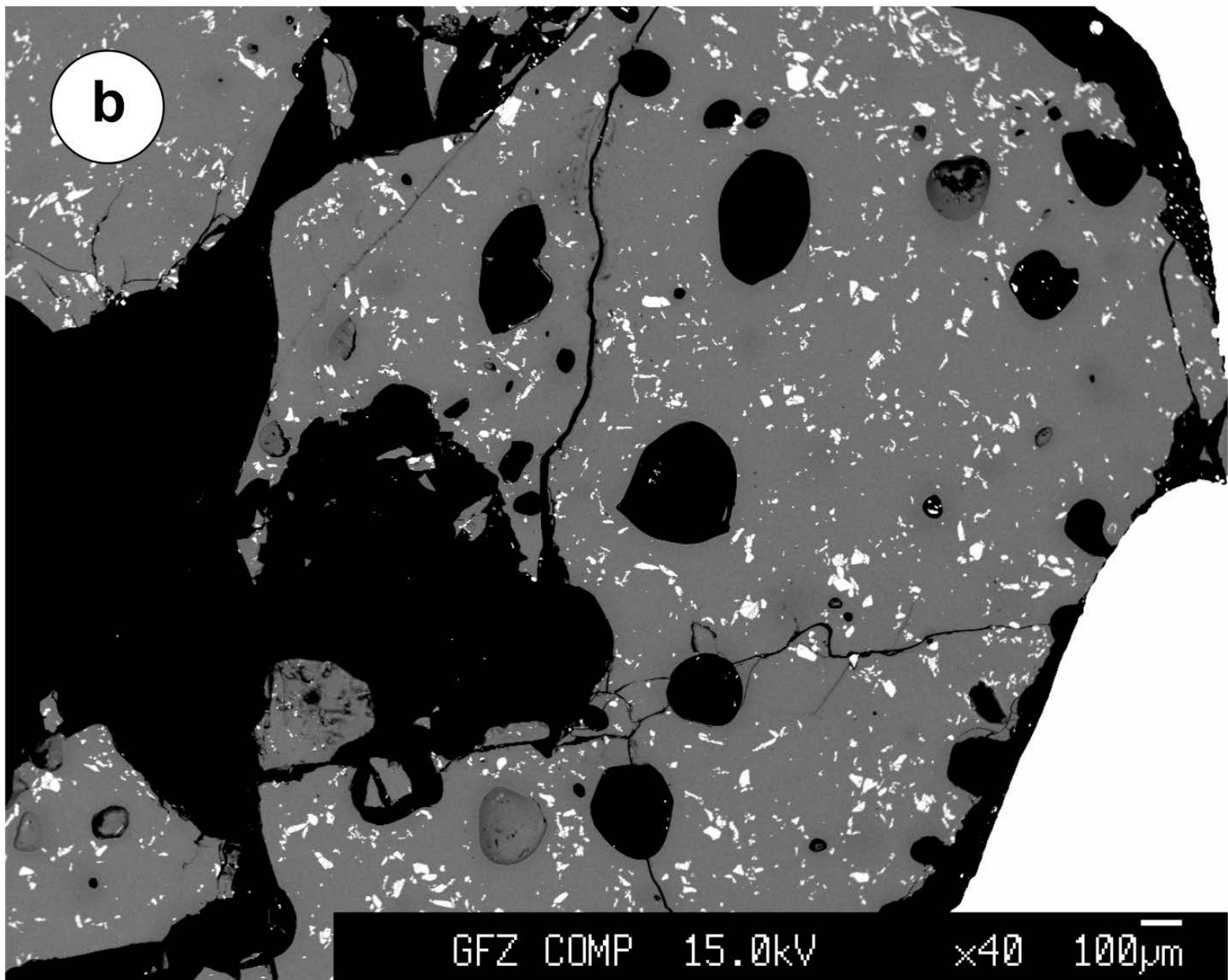
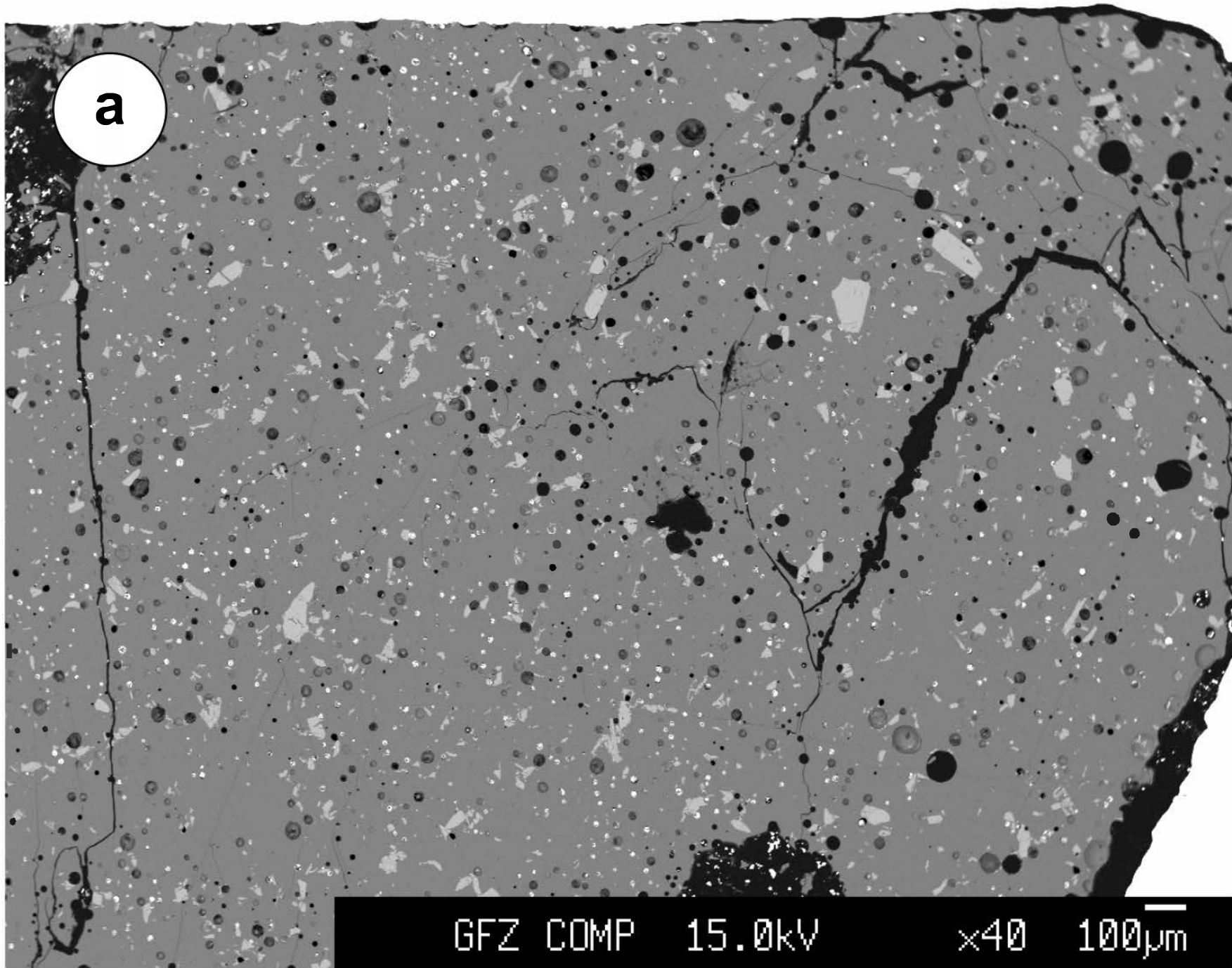


Figure 6.

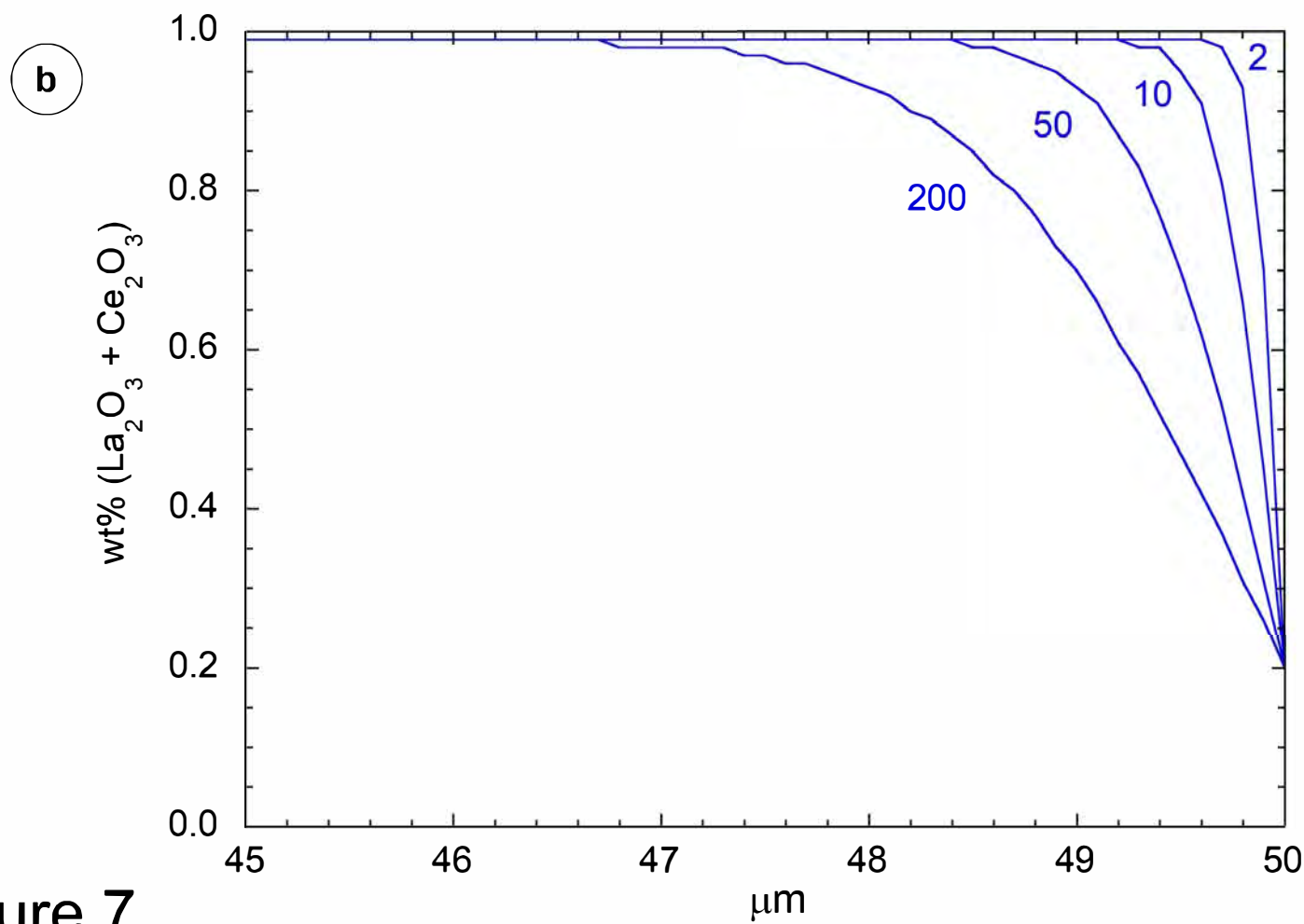
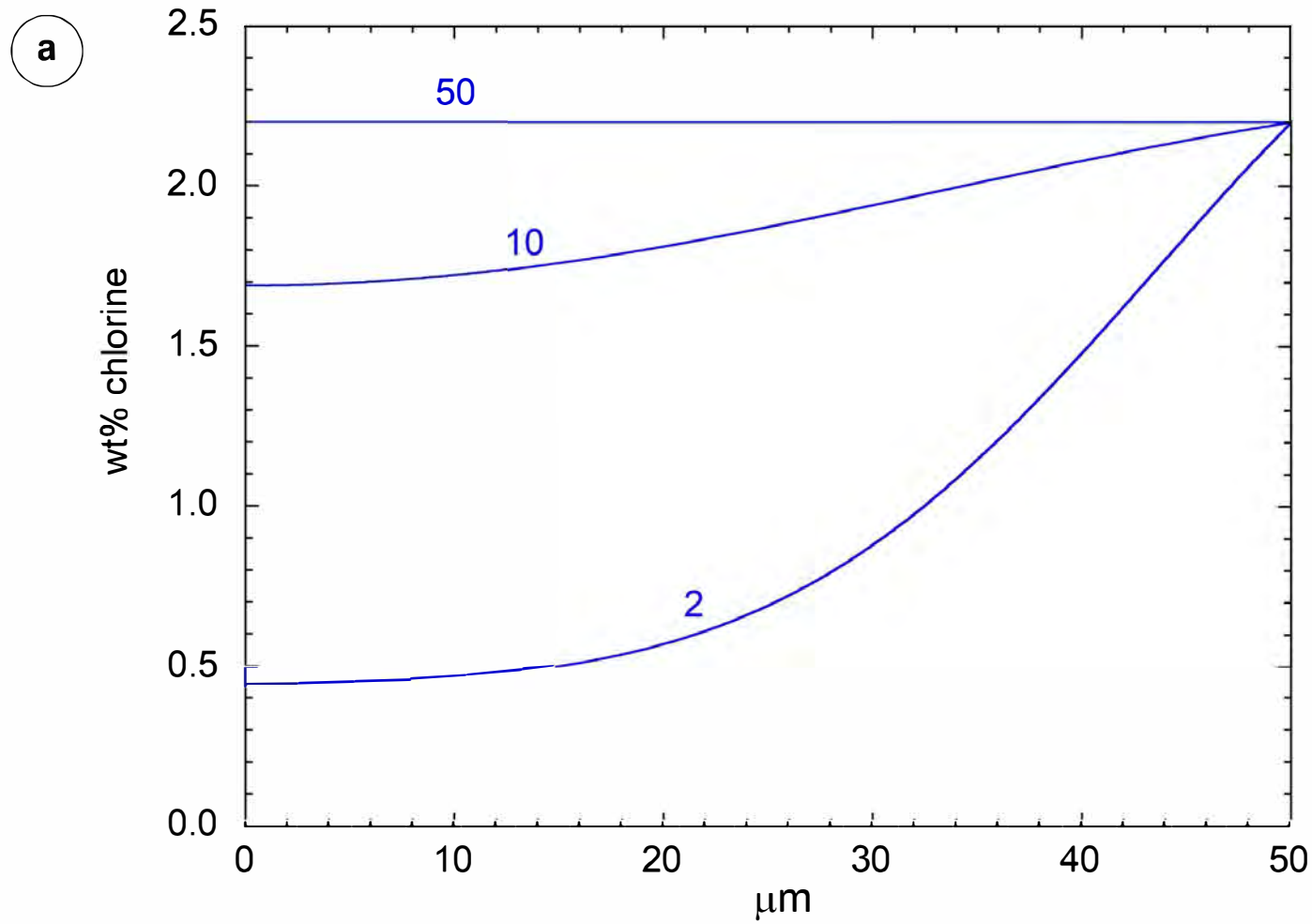


Figure 7.

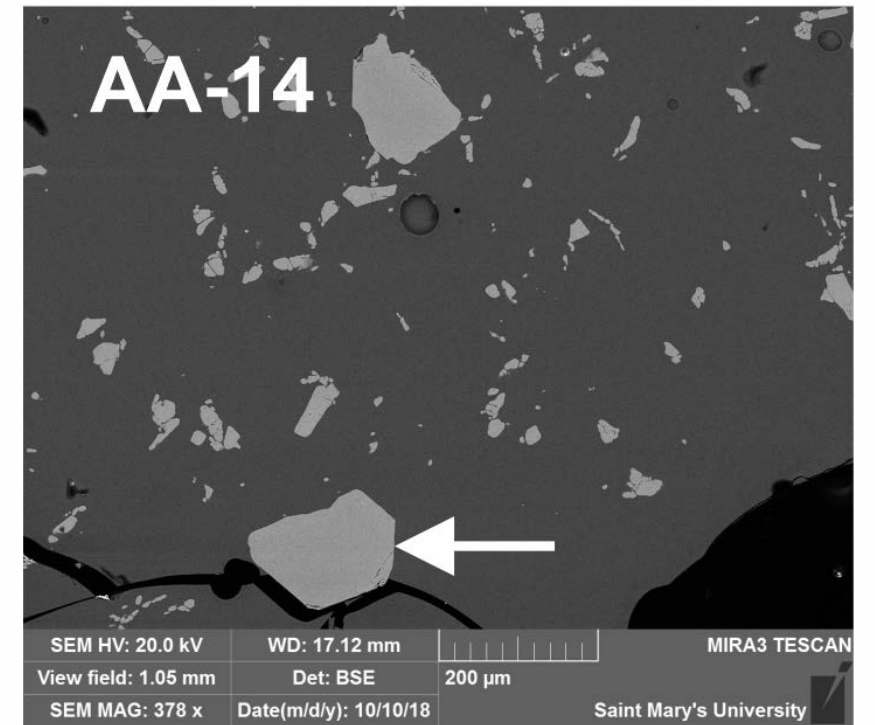
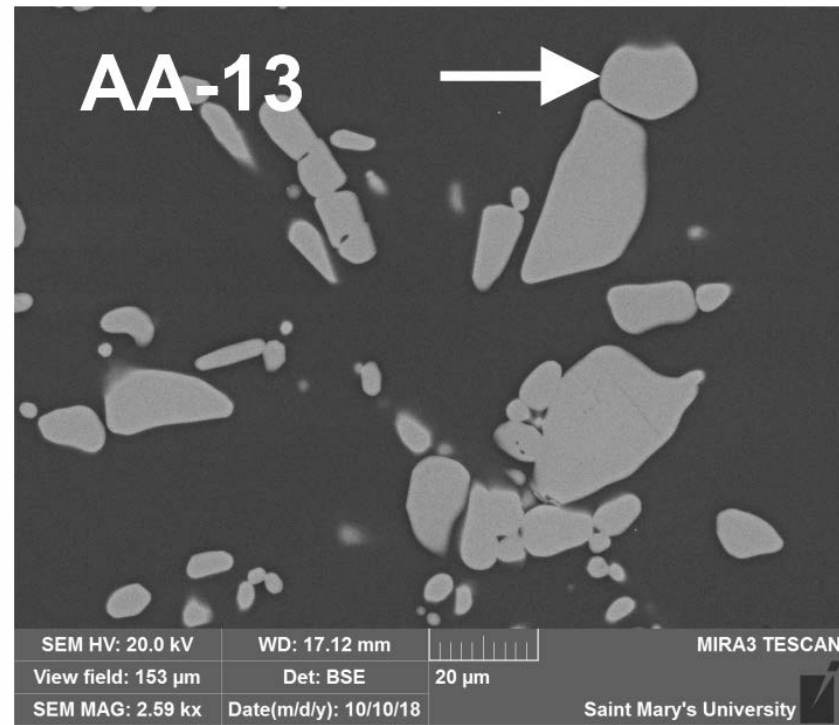
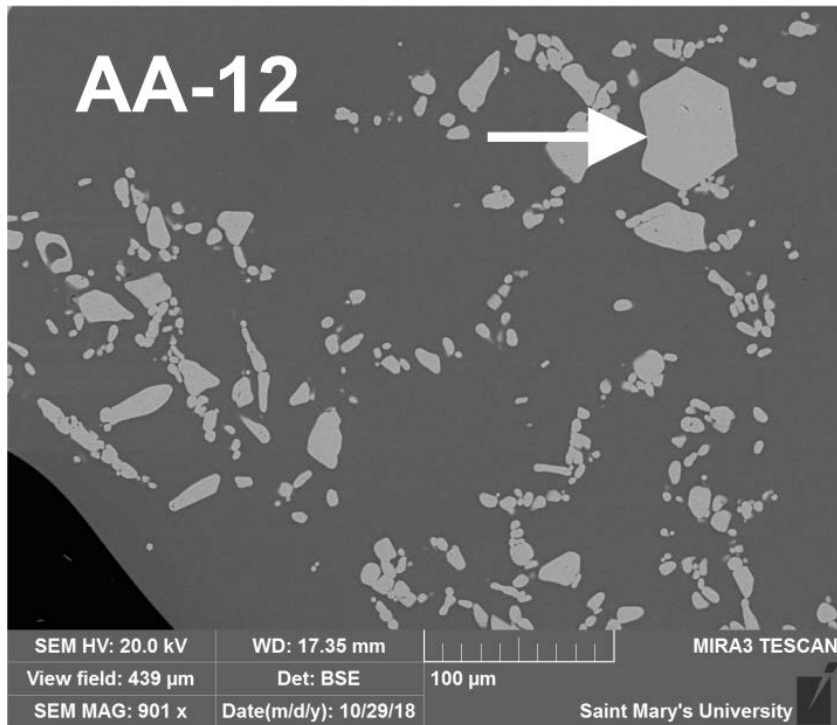
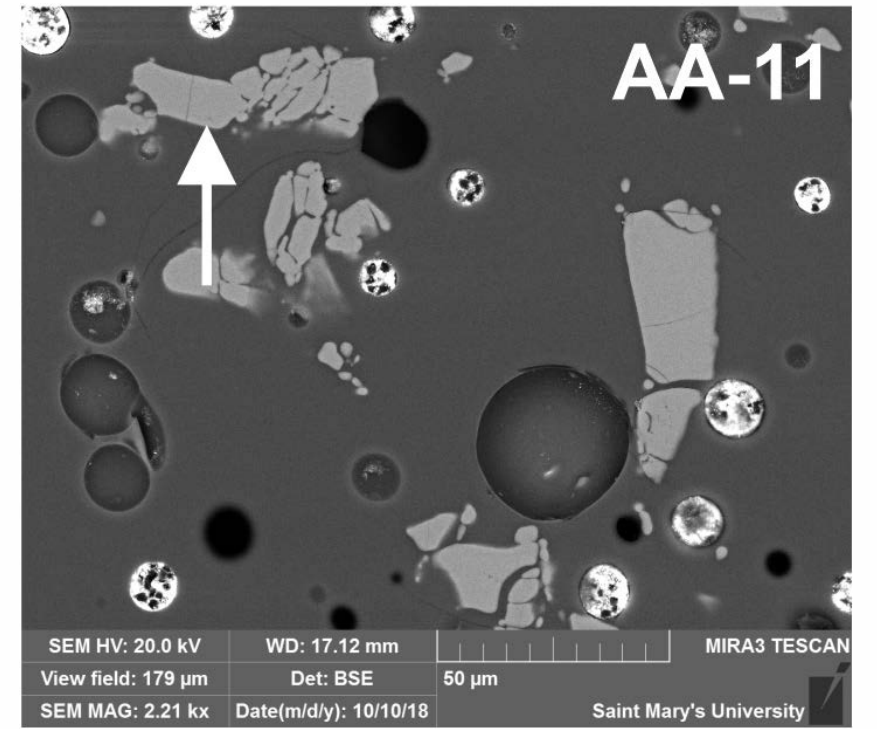
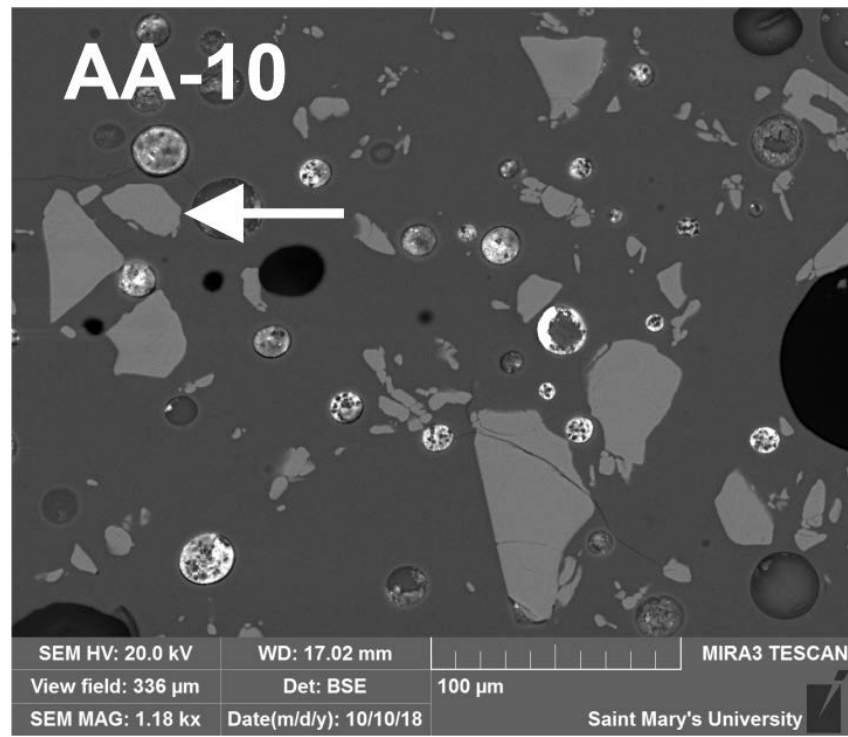
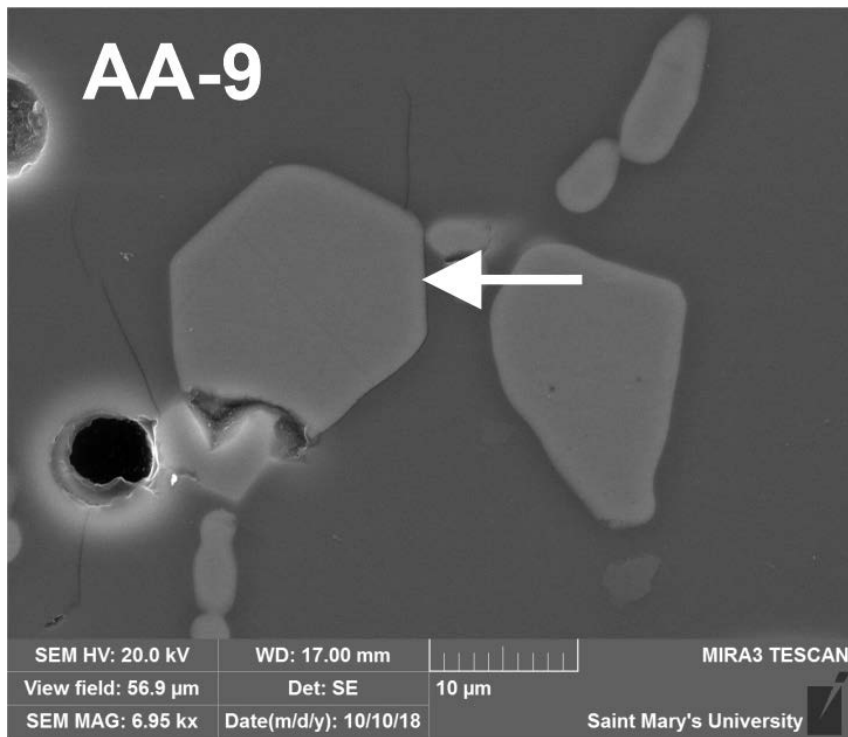


Figure 8.

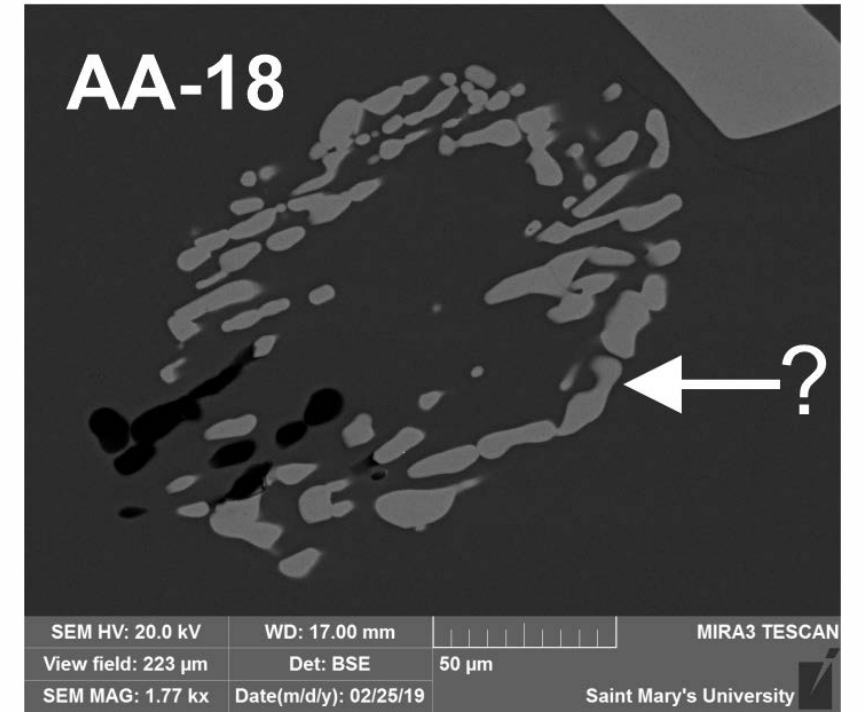
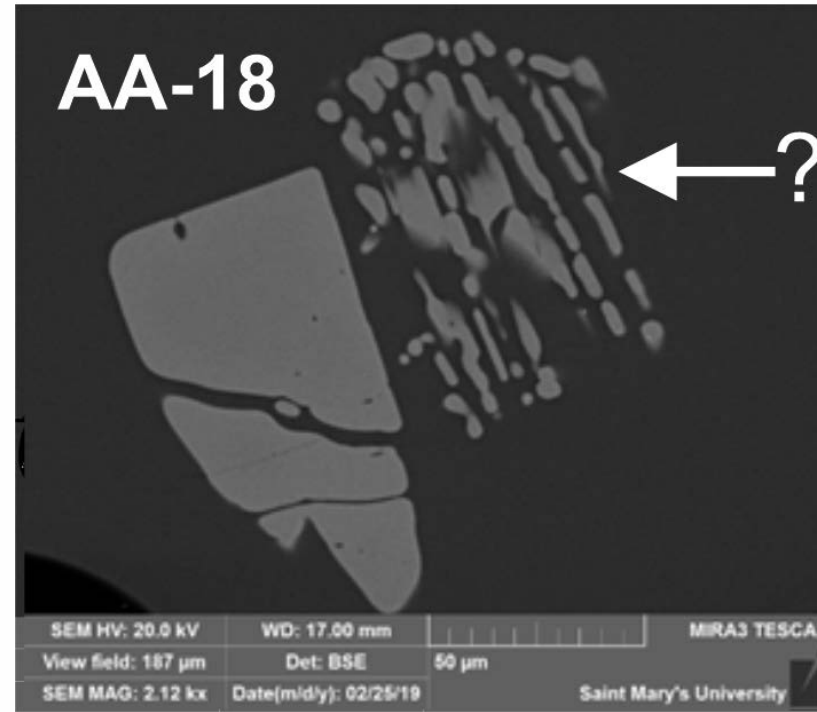
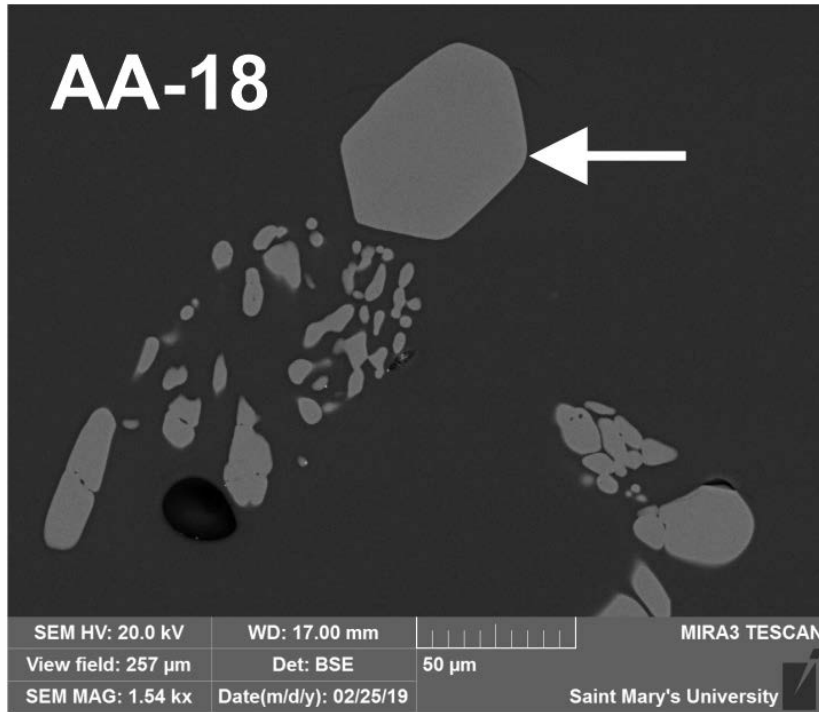
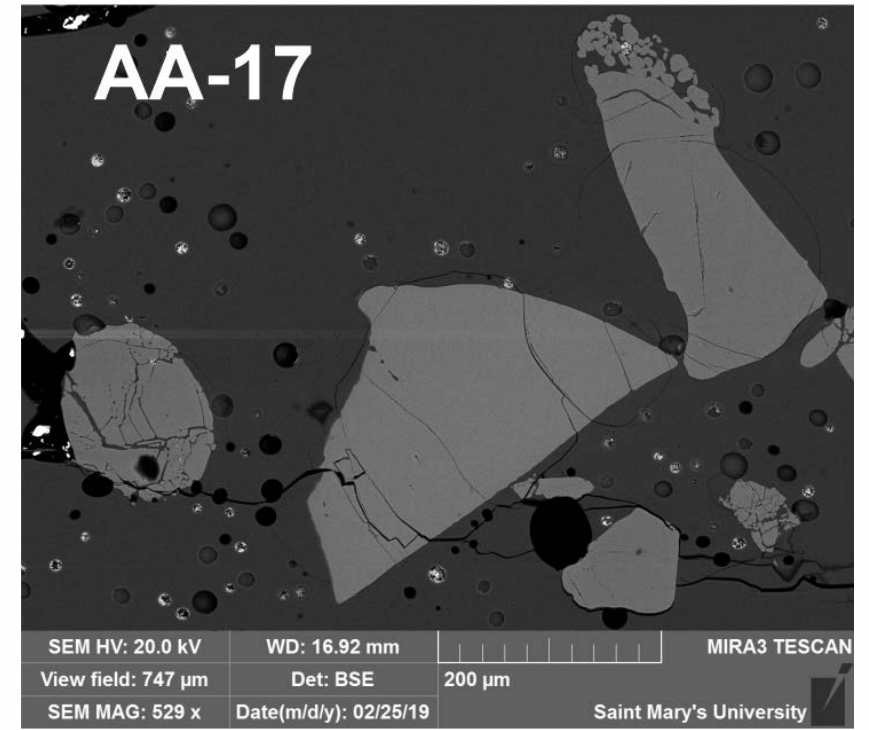
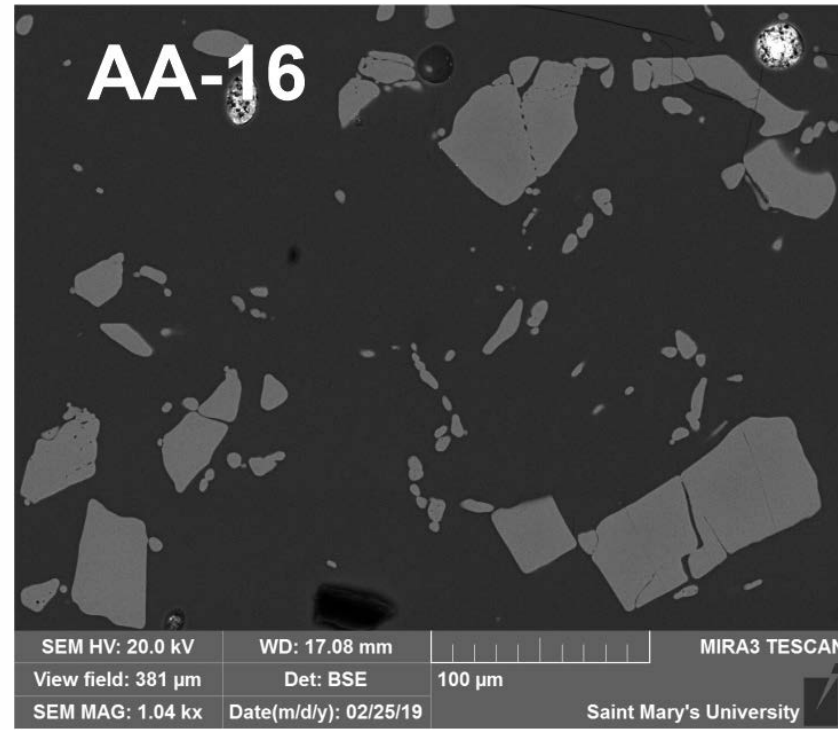
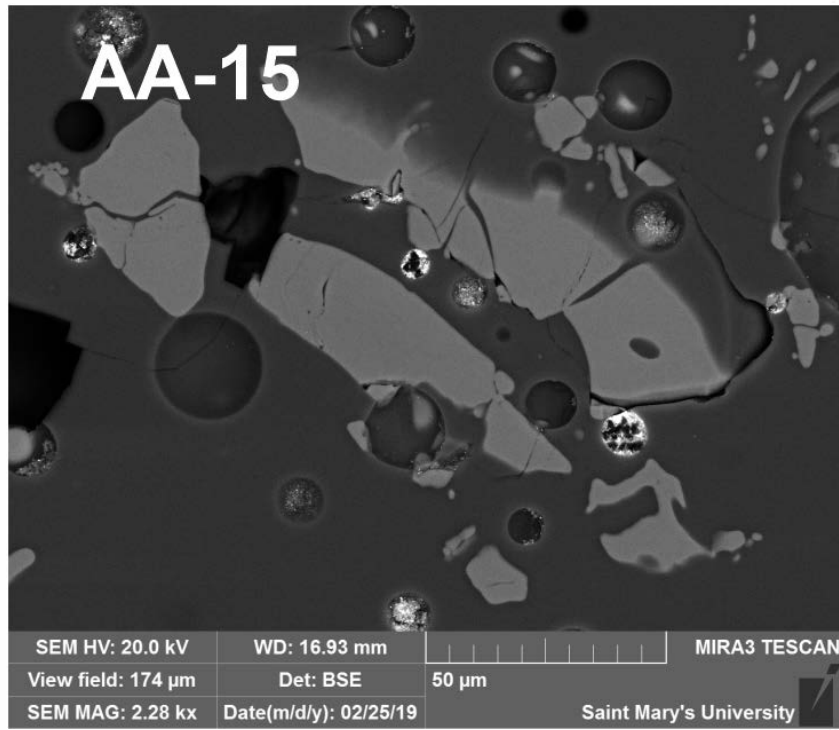


Figure 9.

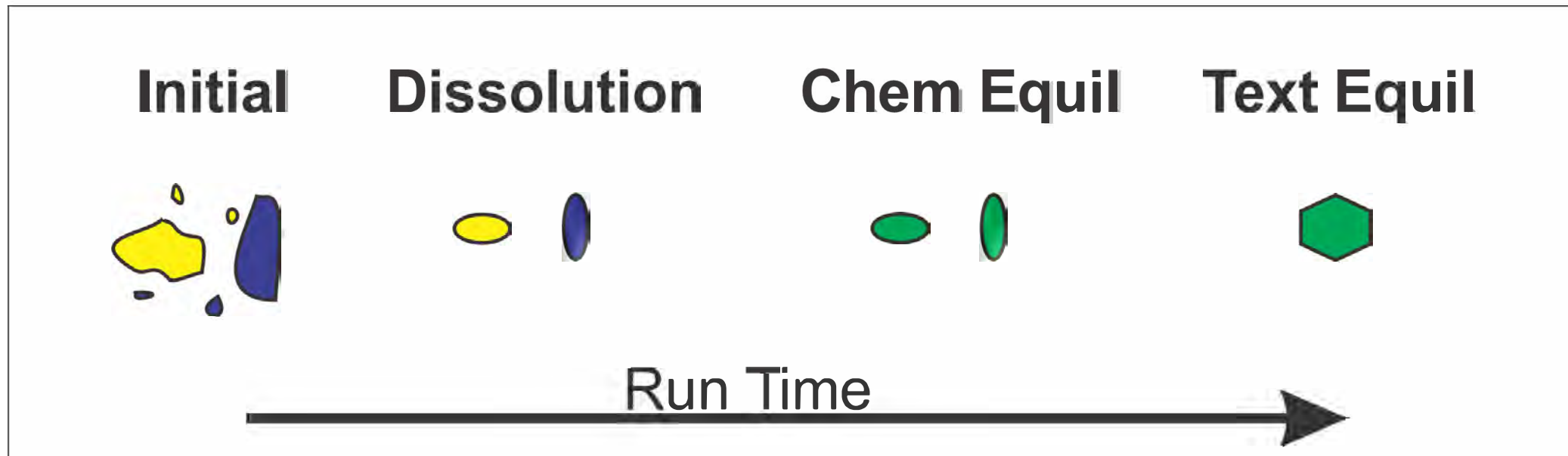


Figure 10.

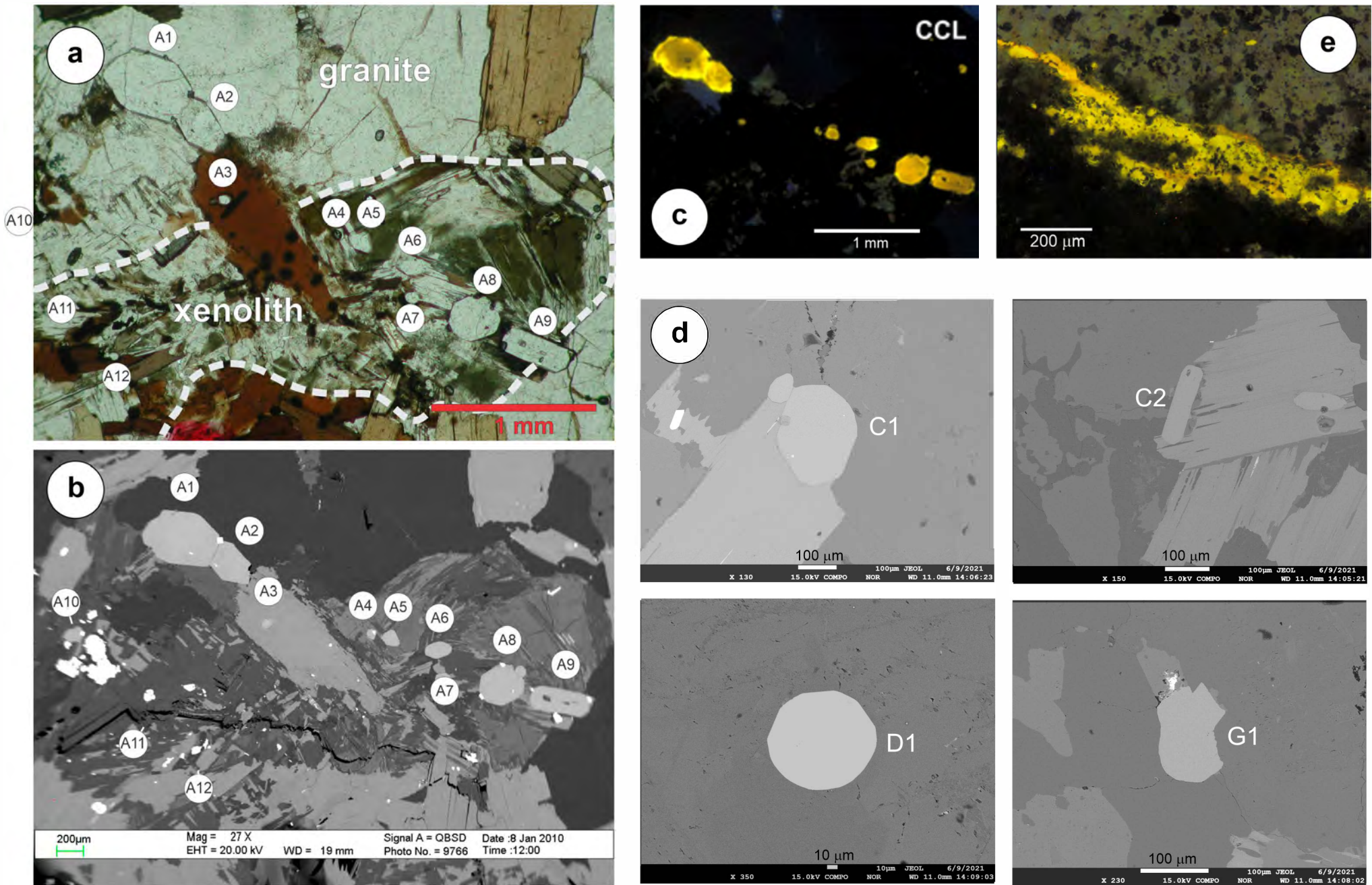


Figure 11.

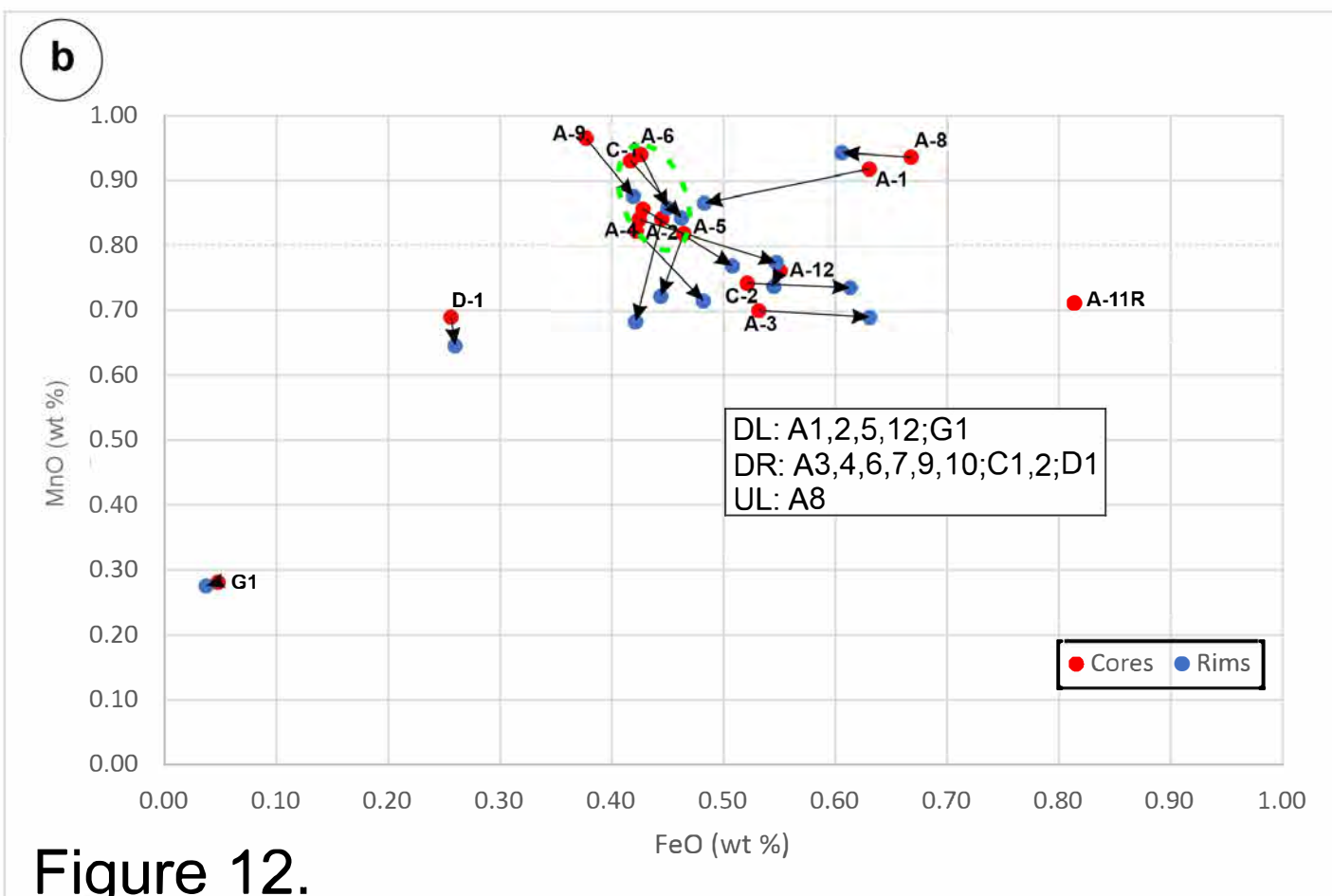
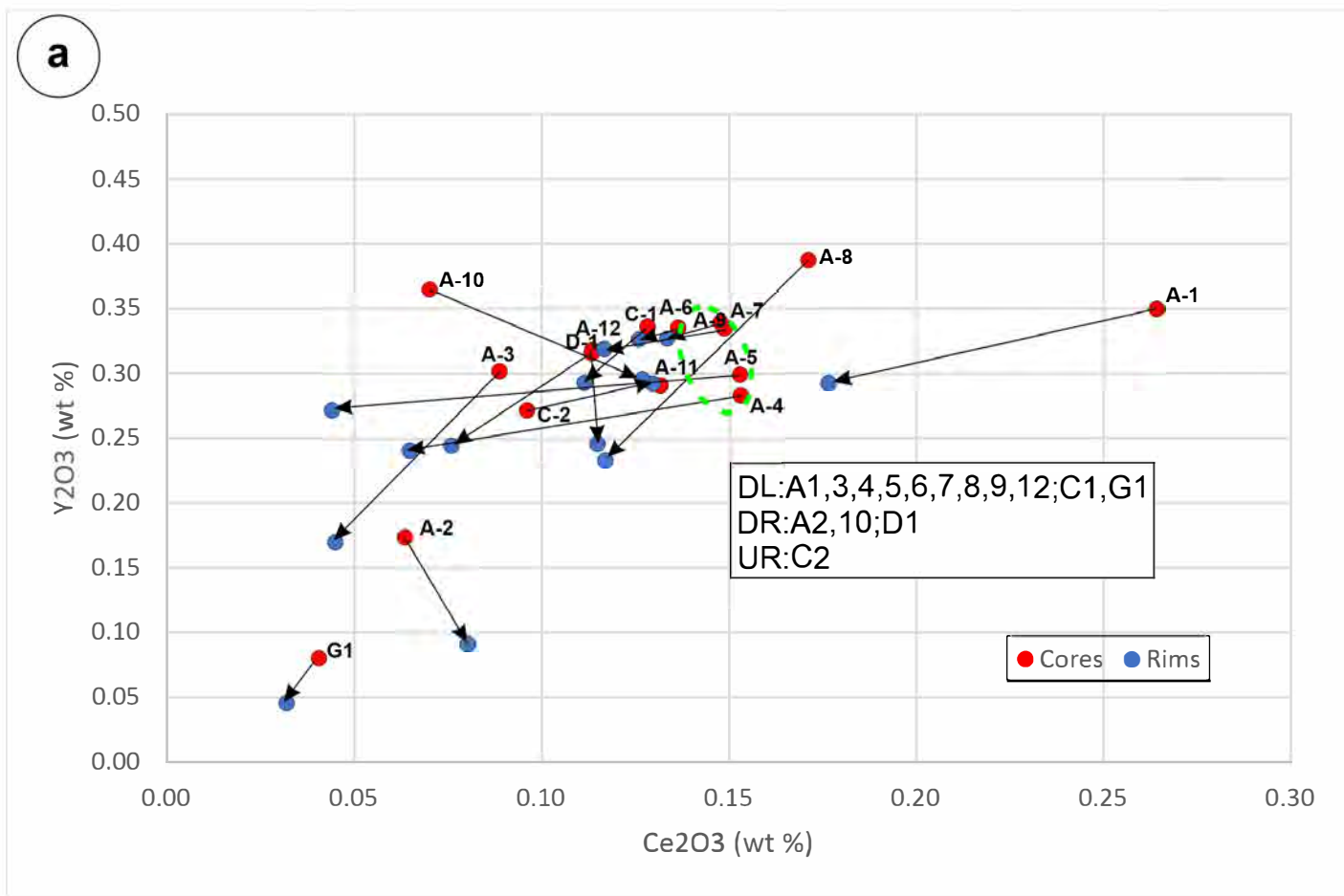


Figure 12.